GREAT AUSTRALIAN BIGHT RESEARCH PROGRAM

RESEARCH REPORT SERIES

Asphaltite and tarball surveys

Final Report GABRP Project 5.2

Andrew Ross, Alex Corrick, Christine Trefry, Se Gong, David McKirdy, Tony Hall, Chris Dyt, Zack Angelini, Richard Kempton, April Pickard, Cameron White, Stacey Maslin, David Griffin, John Middleton, John Luick, Stephan Armand, Tania Vergara and Richard Schinteie

GABRP Research Report Series Number 25a

October 2017

DISCLAIMER

COPYRIGHT

THIS PUBLICATION MAY BE CITED AS:

Ross, A., Corrick, A., Trefry, C., Gong, S., McKirdy, D., Hall, T., Dyt, C., Angelini, Z., Kempton, R., Pickard, A., White, C., Maslin, S., Griffin, D., Middleton, J., Luick, J., Armand, S., Vergara, T. and Schinteie, R. (2017). Asphaltite and tarball surveys. Final Report GABRP Project 5.2. Great Australian Bight Research Program, GABRP Research Report Series Number 25a, 321pp.

CONTACT

Dr Andy Ross
CSIRO
e: Andrew.Ross@csiro.au

FOR FURTHER INFORMATION

www.misa.net.au/GAB

GREAT AUSTRALIAN BIGHT RESEARCH PROGRAM

The Great Australian Bight Research Program is a collaboration between BP, CSIRO, the South Australian Research and Development Institute (SARDI), the University of Adelaide, and Flinders University. The Program aims to provide a whole-of-system understanding of the environmental, economic and social values of the region; providing an information source for all to use.

Contents

LIST OF FIGURES vii

LIST OF TABLES xix

ACKNOWLEDGEMENTS xxi

EXECUTIVE SUMMARY 1

Part I Introduction 3

INTRODUCTION 4

- Overview 4
- Background and need 4
- Objectives 5

REGIONAL GEOLOLOGY OF THE BIGHT BASIN 6

- Basin Outline 6
- Basin evolution and tectonostratigraphic framework 7
- Exploration history 11
- Petroleum geology 11
- Source rocks 12
- Hydrocarbon indications and shows 14
- Box 1 16
- Summary findings of GABRP Project 5.3 fluid Inclusions project 16
- Historical bitumen strandings 18
- Evidence for seeps 21
  - Remote sensing and seismic studies 21
  - Vessel-based investigations 22
- Box 2 26
- Seepage indicators from GABRP Project 5.1 seeps and leakage project. 26
- Formation of coastal bitumen and potentially analogous systems 26
- Proposed origin processes for South Australian asphaltites and waxy bitumen 27
  - Proposed origin of waxy bitumen 27
  - Proposed origin of asphaltites 27
- Potential Analogues 30
  - The Gulf of Mexico 30
  - Santa Barbara Channel, offshore California 33

Part 2 Beach survey data 36

BEACH SURVEY DATA 37
Historical sites studied 37
Beach survey rationale and hypothesis 38
Beach selection approach 39
Beach visit seasons 41
Survey methodologies 46
Logging and sample collection 46
Materials and metadata logged 49
Regional data interpretation 53
Sample numbers and family 54
Stranding locations 58
Stranding position on beach 58
Stranding beach slope and width 63
Beach aspect 64
Detailed interpretation of example beaches 71
Number 1 & 2 rocks 71
Beachport Conservation Park 74
Tractor beach 77
Dogfence Beach 80
Conceptual processes for beach strandings 83
Distribution and occurrence of asphaltites and tarballs on the shoreline of South Australia 84
Summary and conclusions 88
Part 3 Geochemistry 89
INTRODUCTION 90
ANALYTICAL RATIONALE AND METHODS 90
SAMPLE PROCESSING 91
Physical documentation 91
Bulk geochemical screening 92
Percentage of carbon, hydrogen, nitrogen and sulphur using elemental analysis 92
Preliminary oil family fingerprinting and degradation assessment using whole oil full scan gas chromatograph mass spectrometry 92
Carbon and sulphur isotopic compositions using elemental analysis - isotope ratio mass spectrometry (EA-IRMS) 94
Detailed geochemical analyses 95

Fractionation by liquid chromatography 96
Molecular sieve fractionation of branched and cyclic saturated hydrocarbons 97
Saturated fraction biomarker analysis using selected ion monitoring (SIM) gas chromatograph mass spectrometry 98
Saturated fraction biomarker analysis using gas chromatography coupled to tandem mass spectrometry (gc-ms-ms) with cold electron ionisation 101
Aromatic fraction biomarker analysis using gas chromatography mass spectrometry (gc--ms) 101
Carbon isotopic composition of specific hydrocarbons using compound specific isotope analysis (CSIA) 102
OIL FAMILIES FROM BULK GEOCHEMICAL SCREENING 104
Classification of Coastal Bitumen 104
Visual Classification of Stranded Materials 104
Asphaltites 104
Waxy Bitumen 104
Coastal Resin/Amber 106
Sooty Bitumen 107
Polycyclic Aromatic Hydrocarbons 108
Soft Bitumen 108
Bulk Geochemical Classification 109
Key Whole Oil Classifications for Coastal Bitumen Strandings 112
Other Whole Oil Families 113
Limitations of a whole-oil classification scheme 117
BIOMARKER CHARACTERISATION 117
Statistical treatment and interpretation 117
Geochemical grouping 117
Comparison with fluid inclusion oils 161
Biomarker Families Sub-division 166
Asphaltite and Number 1 & 2 Rocks soft bitumen 167
Type I Waxy Bitumens (High Botryococcane) 171
Type II Waxy Bitumens (Low Botryococcane) 173
Type III Waxy Bitumens (No Botryococcane, Low Wax) 175
Type IV Waxy Bitumens (No Botryococcane, High Wax) 185
Sandy River soft bitumens 195
Comparison with Statistical Data Treatment (HCA) 197
Comparison with other data sets 198

Comparison with Indonesian oil families 201
Potential GAB sources 211
Summary and conclusions 214
DEGRADATION OF OIL FAMILIES 214
The need to define the extent of degradation in coastal bitumen 214
Oil family identification: 214
Oceanographic provenance modelling: 214
Historical continuity 215
Introduction to hydrocarbon degradation 215
Biodegradation 216
Water washing 217
Evaporation 218
Photo-oxidation 218
Asphaltite Degradation 218
Visual and physical characteristics of degradation 218
Approach to degradation assessment 219
Whole oil GC-MS 219
Compound Specific Isotope Analysis 221
Asphaltite Biomarker Degradation Assessment 224
Degradation of waxy bitumen 226
Visual and physical characteristics of degradation 226
Approach to degradation assessment 227
Degradation of Type I waxy bitumen (high botryococcane) 229
Historical continuity 229
Degradation of Type II waxy bitumen (low botryococcane) 232
Historical continuity 232
Degradation of Type III waxy bitumen (no botryococcane, low wax) 234
Historical continuity 234
Degradation of Type IV waxy bitumen (no botryococcane, high wax) 235
Historical continuity 236
Miscellaneous types of coastal bitumen (unknowns, unclassified high wax bitumen) 236
Waxy bitumen biomarker degradation 238
Summary and conclusions 240
GEOCHEMISTRY SUMMARY AND CONCLUSIONS 241

Part 4 Oceanography 243

IMPLICATIONS OF METOCEAN CONDITIONS OF THE GAB ON ASPHALTITE AND TARBALL STRANDINGS 244

Introduction to metocoean conditions of the Great Australian Bight 244

Meteorological conditions of the Great Australian Bight 244

Predominant regional currents 248

The Flinders Current 248

The Leeuwin Current 249

Coastal Current 249

Mesoscale Eddies 249

Other oceanographic processes 250

Upwelling 250

Downwelling 251

El-Nino - La Nina Effects (ENSO) 252

Surface Waves and Tides 252

Oceanographic modelling of asphaltite and tarball strandings in Great Australian Bight 254

Rationale and hypothesis 254

Oceanographic models 255

Global Models 255

Regional Models 256

Model parameterisations 259

Scenario 1 – Comparison of winter and summer offshore seeded particle trajectories using currents only 259

Scenario 2 – Offshore seeded particle trajectories using currents and wave movement 259

Scenario 3 - Back track trajectories from beach seeding locations using currents and wave movement 261

Oceanographic modeling results 263

Scenario 1 - Comparison of winter and summer offshore seeded particle trajectories using currents only 263

Scenario 2 - Offshore seeded particle trajectories using currents and Stokes drift 269

Scenario 3 – Back track models 279

Discussion of oceanographic modeling results 286

Oceanographic modelling summary and conclusions 288

Part 5 Conclusion 291

CONCLUSIONS 292

REFERENCES 294
Part 6 Appendices 311
APPENDIX 1: DATA MANAGEMENT 312
Raw datasets created 312
Data processing and derived datasets 312
Data curation and archive 312
Data access, use agreements and licensing 312
Publication of datasets 312
APPENDIX 2: STUDENT PROJECTS 313
Student name 313
Degree type, project title and institution 313
Status of student project 313
APPENDIX 3: PROJECT PUBLICATIONS 313
Papers 313
Presentations 313
Patents 313
Media releases 313
APPENDIX 4: INTELLECTUAL PROPERTY 313
Unique discoveries 313
Action plan 314
APPENDIX 5: BEACH DOSSIERS 314
APPENDIX 6: SAMPLE REPORTS 314
APPENDIX 7: SAMPLE ANALYSIS DATA 314
APPENDIX 8: BRAN MAPS FOR 2011, 2012 and 2013 315

LIST OF FIGURES

Figure 1: Location of the Bight Basin with component sub-basins. © Commonwealth of Australia (Geoscience Australia) 2016. ... 6
Figure 2: Cross-section through the eastern Madura Shelf and Ceduna Sub-basin. From Bradshaw et al., 2003. ... 8
Figure 3: Cross-section through the eastern Madura Shelf, Ceduna Sub-basin and eastern Recherche Sub-basin. From Bradshaw et al., 2003. ... 9
Figure 4: Cross-section through the eastern Madura Shelf, Ceduna Sub-basin and eastern Recherche Sub-basin. From Bradshaw et al., 2003. ... 9
Figure 5: Bight Basin stratigraphic correlation chart showing basin phases and predicted source rock intervals (modified from Blevin et al., 2000 and Totterdell et al., 2000). The sea level curve (Haq et al., 1988) is modified to the time scale of Gradstein et al., 2004. ... 10
Figure 6: Location of bitumen stranding sites along the Australian coastline (after Edwards et al. 2016). ... 19
Figure 7: Stranding locations of coastal bitumen in South Australia and western Victoria (after Edwards et al. 2016). ... 20
Figure 8: Combined historical and capture program (SAR Slick Features) sea surface synthetic aperture radar anomalies for the Great Australian Bight, plus seismic indications of fluid escape in the Duntroon sub-basin. ... 22
Figure 9: Combined historic seafloor sampling sites from surveys undertaken in the Great Australian Bight. ... 23
Figure 10: Bight Basin Sampling and Seepage Survey SS01/2007: survey areas and location of sampling sites (Totterdell & Mitchell, 2009). ... 24
Figure 11: Surface ocean currents responsible for the transport of coastal bitumen from Southeast Asia to southern Australia (after Edwards et al., 2016; Padley 1995). ... 28
Figure 12: Simplified model for submarine canyon incision resulting in lateral bituminous seeps from subsurface tar mats. (A) Source rocks deposited in the basin are buried at sufficient depth to generate hydrocarbons which migrate along a carrier bed. Asphalts precipitated from produced oils due to pressure changes during migration (Wilhelms & Larter, 1995), forming viscous sub-surface tar mats, while the oil charge either migrates to a viable trap or is lost due to a lack of a sealing unit. (B) Slumping at the shelf edge results in submarine canyon incision, exposing the subsurface asphaltic tar mats. After the bitumen has become fragmented, upwelling currents which travel up the submarine canyon are then able to entrain pieces of this bitumen resulting in their transportation to the shallower regions of the shelf. ... 29
Figure 13: Examples of seafloor expressions of asphaltic bitumen from the Gulf of Mexico. (A) Seafloor asphalt mounds and flows from Chapopote Knoll, Southern Gulf of Mexico after Brüning et al., (2010). (B) Fragmented seafloor asphalt from Chapopote Knoll, Southern Gulf of Mexico after Brüning et al., (2010). (C) – (F) Examples of seafloor expression of hydrocarbon seeps in the Gulf of Mexico after Sahling et al., (2016). ... 31
Figure 14: Overview of asphaltic bitumen spreading and fragmentation based on studied sites at Chapopote Knoll after Brüning et al., (2010). Continual weathering and loss of volatiles results in surficial cracking and asphalt fragmentation. ... 32
Figure 15: Comparison of fracture patterns in asphaltic flows in the Gulf of Mexico and the South Australian coastal asphaltites. (A+B) ROV QUEST images of fractured asphalt at Chapopote Knoll

modified after Brüning et al., (2010). Yellow annotation lines highlight the clearly preferred fracture orientation. (C) South Australian asphaltite sample W13/007507, an example of the highly fractured asphaltite surface. (D) Asphaltite sample W13/007507 with fracture orientations annotated in yellow lines. 33
Figure 16: Examples of seafloor tar seepage and sea surface tar formation from offshore California. Photographs A-E after Lorenson et al., (2009). (A) Remotely operated vehicle (ROV) image of extruding tar mound. (B) A 'tarwhip' extruding from a seafloor tar mound. (C) Viscous tar floating on the sea surface offshore from Point Conception on the southern coast of Santa Barbara, California. (D) Collected viscous tar from sea surface from Point Conception on the southern coast of Santa Barbara, California. (E) Natural oil slick forming tar patties observed on the sea surface offshore from California. (F) Overview of tar mound formation for offshore California after Woods Hole Oceanographic Institution <http://www.whoi.edu/oilinocean/page.do?pid=51880&tid=441&cid=107898&ct=61&article=73026>. 35
Figure 17: Beaches visited during the 2014 / 2015 / 2016 seasons. 41
Figure 18: Project 5.2 team walking the upper-beach during the survey. 47
Figure 19: Investigation of a bitumen sample. 48
Figure 20: Data entry form for the CSIRO developed beach survey database system. 49
Figure 21: Sample numbers plotted against oil family (determined by whole oil GC-MS) by year after exclusion of donated samples plus unclassifiable and miscellaneous materials. 56
Figure 22: Stranding position on beach. 59
Figure 23: 2014 tides at Thevenard, South Australia. 60
Figure 24: 2014 wind speeds at Thevenard, South Australia. 60
Figure 25: 2015 tides at Thevenard, South Australia. 61
Figure 26: 2015 wind speeds at Thevenard, South Australia. 61
Figure 27: 2016 tides at Thevenard, South Australia. 62
Figure 28: 2016 wind speeds at Thevenard, South Australia. 62
Figure 29: Stranding by beach slope. 63
Figure 30: Beach widths. 64
Figure 31: Beach aspect. 65
Figure 32: Beach aspect and sample numbers. 67
Figure 33: Rose diagrams of gross sample numbers by beach aspect (top row) and sample numers normalised by beach aspect (g/100m, bottom row) plotted by survey year for bitumen and asphaltites (donated samples and unclassifiable and miscellaneous materials excluded). 68
Figure 34: Rose diagrams of gross sample loadings by beach aspect (top row) and normalised sample loadings b beach aspect (g/100m, bottom row) by survey year for bitumen and asphaltites (donated samples and unclassifiable and miscellaneous materials excluded). 69
Figure 35: Rose diagrams of total numbers by percent (top row) and sample loadings by percentage (bottom row) plotted by aspect and by survey year for bitumen and asphaltites (donated samples and unclassifiable and miscellaneous materials excluded). 70
Figure 36: Satellite image of the Number 1 & 2 Rocks beach with surveys extents undertaken and locations of samples collected by year. 72
Figure 37: Images taken of the beach for each year for the Number 1 & 2 Rocks beach surveys. 72
Figure 38: Compilation of beach survey data graphs for Number 1 & 2 Rocks. 73

Figure 39: Satellite image of the Beachport Conservation Park beach with surveys extents undertaken and locations of samples collected by year. 75
Figure 40: Images taken of the beach for each year for the Beachport Conservation Park beach surveys. 75
Figure 41: Compilation of beach survey data graphs for the Beachport Conservation Park beach. 76
Figure 42: Satellite image of Tractor Beach with surveys extents undertaken and locations of samples collected by year. 78
Figure 43: Images taken of the beach for each year for the Tractor Beach surveys. 78
Figure 44: Compilation of beach survey data graphs Tractor Beach. 79
Figure 45: Satellite image of Dogfence Beach with surveys extents undertaken and locations of samples collected by year. 81
Figure 46: Images taken of the beach for each year for the Dogfence Beach surveys. 81
Figure 47: Compilation of beach survey data graphs Dogfence Beach. 82
Figure 48: Conceptual framework for collection of materials on wave-dominated beaches with open shoreline aspects. 83
Figure 49: Conceptual framework for collection of materials on wave-dominated beaches with restricted shoreline aspects. 84
Figure 50: Hydrocarbon loadings along the South Australian coastline from coastline surveys between 1990 and 2016. Note that the 1990 and 1991 surveys shown were only for six selected beaches along the limestone coast. 85
Figure 51: Total asphaltite strandings and distribution per year. 86
Figure 52: Total bitumen (tarball) strandings and distribution per year on a log scale. 86
Figure 53: Distribution of asphaltite and main waxy bitumen families plotted to scale according to number of samples. 87
Figure 54: Pasteur pipette configuration for separation of saturated, aromatic and polar fractions. 97
Figure 55: Examples of asphaltite. (A) Sample W13/007507. (B) Sample W13/007672. (C) Sample W13/007473. (D) Sample W13/007742 opened in half, demonstrating the characteristic conchoidal fracture exhibited by the asphaltites. (E) Sample W13/007976, the largest and freshest asphaltite collected (3.3 kg with a soft interior). 105
Figure 56: Examples of waxy bitumen. (A) Sample W13/007700. (B) Sample W13/007697. (C) Sample W13/007521. (D) Sample W13/007521 cut in half to reveal black interior. (E) Sample W13/007680. (F) W13/007683. (G) Sample W13/007601. 106
Figure 57: Examples of coastal amber/resins. (A) Sample W13/007555. (B) Sample W13/007645. (C) Sample W13/007761. (D) Sample W13/007555. 107
Figure 58: Sample W13/007518 of sooty bitumen. 108
Figure 59: Sample W13/007768C, comprised of pure polycyclic aromatic hydrocarbons. 108
Figure 60: Examples of soft bitumen found in 2016. (A) Sample W13/007923 collected from Sandy River. Note the sample was flattened from storage in an aluminium sleeve. (B) Soft bitumen collected from Number 1 and 2 Rocks. 109
Figure 61: Whole-oil GC-MS total ion chromatograms of the freshest examples of the key whole-oil families for the South Australian coastal bitumen. (A) Asphaltite, sample W13/007976. (B) Type I waxy bitumen (high botryococcane), sample W13/007601. (C) Type II waxy bitumen (low botryococcane), sample W13/007615. (D) Type III waxy bitumen (no botryococcane, low wax), sample W13/007697. (E) Type IV waxy bitumen (no botryococcane, high wax), sample W13/007589. 111

Figure 62: Whole oil GC-MS total ion chromatogram for unclassified high wax sample COA/000963. In this sample clear response peaks only remain for n-alkanes ≥ C34, limiting a descriptive classification. 113
Figure 63: Whole oil GC-MS total ion chromatogram for resin sample W13/007471. 114
Figure 64: Whole oil GC-MS total ion chromatogram for sooty bitumen sample W13/007518. 114
Figure 65: Whole oil GC-MS total ion chromatogram for polycyclic aromatic hydrocarbon sample W13/007768C. 115
Figure 66: Whole oil GC-MS total ion chromatogram for Sandy River soft bitumen sample W13/007923. 115
Figure 67: Whole oil GC-MS total ion chromatogram for degraded asphaltite sample W13/007663. 116
Figure 68: Whole oil GC-MS total ion chromatogram for Number 1 and 2 Rocks soft bitumen sample /001079. 116
Figure 69: Total Ion chromatograms of representative whole oil samples which were heavily biodegraded. 119
Figure 70: Dendrogram of the hierarchical cluster analysis (HCA) of 32 source variables showing different groups of asphaltite and waxy bitumen samples. 120
Figure 71: Partial dendrogram of the hierarchical cluster analysis of Group 1 samples in Figure 70.124
Figure 72: Partial *m/z* 191 mass chromatograms of representative Type I waxy bitumens (7898 and 7999) and Type IV waxy bitumen (7857A) in Group 1 showing the distribution of tricyclic terpanes and hopanes. For peak identifications refer to table 18. 125
Figure 73: Partial *m/z* 205 mass chromatograms of representative Type I waxy bitumens (7898 and 7999) and Type IV waxy bitumen (7857A) in Group 1 showing the distribution of methylhopanes. For peak identifications refer to table 18. 126
Figure 74: Partial *m/z* 217 mass chromatograms of representative Type I waxy bitumens (7898 and 7999) and Type IV waxy bitumen (7857A) in Group 1 showing the distribution of steranes and diasteranes. For peak identifications refer to table 19. 127
Figure 75: Partial *m/z* 259 mass chromatograms of representative Type I waxy bitumens (7898 and 7999) and Type IV waxy bitumen (7857A) in Group 1 showing the distribution of diasteranes and tetracyclic polyprenoids. For peak identifications refer to table 19. 128
Figure 76: Partial dendrogram of the hierarchical cluster analysis of Group 2 in Figure 70. 130
Figure 77: Partial *m/z* 191 mass chromatograms of representative Type IV waxy bitumen (7593) and unclassified high wax bitumen (7978) and Type III waxy bitumen (7503) in Group 2 showing the distribution of tricyclic terpanes and hopanes. For peak identifications refer to table 18. 131
Figure 78: Partial *m/z* 217 mass chromatograms of representative Type III waxy bitumen samples (1032, 7683 and 7695) in Group 2 showing the distribution of methylhopanes. For peak identifications refer to table 19. 132
Figure 79: Partial *m/z* 217 mass chromatograms of representative Type III waxy bitumen samples (1032, 7683 and 7695) in Group 2 showing the distribution of steranes and diasteranes. For peak identifications refer to table 18. 133
Figure 80: Partial *m/z* 259 mass chromatograms of representative Type III waxy bitumen samples (1032, 7683 and 7695) in Group 2 showing the distribution of diasteranes and tetracyclic polyprenoids. For peak identifications refer to table 19. 134
Figure 81: Partial dendrogram of the hierarchical cluster analysis of Group 3 in Figure 70. 136

Figure 82: Partial *m/z* 191 mass chromatograms of representative Type IV waxy bitumen (7978) in Group 3 showing the distribution of tricyclic terpanes and hopanes. For peak identifications refer to table 18. 137
Figure 83: Partial *m/z* 205 mass chromatograms of representative Type IV waxy bitumen (7978) in Group 3 showing the distribution of methylhopanes. For peak identifications refer to table 18. 137
Figure 84: Partial *m/z* 217 mass chromatograms of representative Type IV waxy bitumen (7978) in Group 3 showing the distribution of steranes and diasteranes. For peak identifications refer to table 19. 137
Figure 85: Partial *m/z* 259 mass chromatograms of representative Type IV waxy bitumen (7978) in Group 3 showing the distribution of diasteranes and tetracyclic polyprenoids. For peak identifications refer to table 19. 138
Figure 86: Partial dendrogram of the hierarchical cluster analysis of Group 4 in Figure 70. 140
Figure 87: Partial *m/z* 191 mass chromatograms of representative asphaltite (7830), Type IV waxy bitumen (7911), unclassified high wax (7712), Number 1&2 Rocks soft bitumen (1081), degraded asphaltite (7665) and Type II waxy bitumen (7615) in Group 4 showing the distribution of tricyclic terpanes and hopanes. For peak identifications refer to table 18. 141
Figure 88: Partial *m/z* 205 mass chromatograms of representative asphaltite (7830), Type IV waxy bitumen (7911), unclassified high wax (7712), Number 1&2 Rocks soft bitumen (1081), degraded asphaltite (7665) and Type II waxy bitumen (7615) in Group 4 showing the distribution of methylhopanes. For peak identifications refer to table 18. 142
Figure 89: Partial *m/z* 217 mass chromatograms of representative asphaltite (7830), Type IV waxy bitumen (7911), unclassified high wax (7712), Number 1&2 Rocks soft bitumen (1081), degraded asphaltite (7665) and Type II waxy bitumen (7615) in Group 4 showing the distribution of steranes and diasteranes. For peak identifications refer to table 19. 143
Figure 90: Partial *m/z* 259 mass chromatograms of representative asphaltite (7830), Type IV waxy bitumen (7911), unclassified high wax (7712), Number 1&2 Rocks soft bitumen (1081), degraded asphaltite (7665) and Type II waxy bitumen (7615) in Group 4 showing the distribution of diasteranes and tetracyclic polyprenoids. For peak identifications refer to table 19. 144
Figure 91: Partial dendrogram of the hierarchical cluster analysis of Group 5 in Figure 70. 147
Figure 92: Partial *m/z* 191 mass chromatograms of representative Sandy River soft bitumen (7944) and Type IV waxy bitumen (7909) in Group 5 showing the distribution of tricyclic terpanes and hopanes. For peak identifications refer to table 18. 148
Figure 93: Partial *m/z* 205 mass chromatograms of representative Sandy River soft bitumen (7944) and Type IV waxy bitumen (7909) in Group 5 showing the distribution of methylhopanes. For peak identifications refer to table 18. 148
Figure 94: Partial *m/z* 217 mass chromatograms of representative Sandy River soft bitumen (7944) and Type IV waxy bitumen (7909) in Group 5 showing the distribution of steranes and diasteranes. For peak identifications refer to table 19. 149
Figure 95: Partial *m/z* 259 mass chromatograms of representative Sandy River soft bitumen (7944) and Type IV waxy bitumen (7909) in Group 5 showing the distribution of diasteranes and tetracyclic polyprenoids. For peak identifications refer to table 19. 149
Figure 96: Partial dendrogram of the hierarchical cluster analysis of Group 6 in Figure 70. 152
Figure 97: Partial *m/z* 191 mass chromatograms of representative Type I (7962) and Type III waxy bitumen (7910) in Group 6 showing the distribution of tricyclic terpanes and hopanes. For peak identifications refer to table 18. 153

Figure 98: Partial *m/z* 205 mass chromatograms of representative Type I (7962) and Type III waxy bitumen (7910) in Group 6 showing the distribution of methylhopanes. For peak identifications refer to table 18. 153
Figure 99: Partial *m/z* 217 mass chromatograms of representative Type I (7962) and Type III waxy bitumen (7910) in Group 6 showing the distribution of steranes and diasteranes. For peak identifications refer to table 19. 154
Figure 100: Partial *m/z* 259 mass chromatograms of representative Type I (7962) and Type III waxy bitumen (7910) in Group 6 showing the distribution of diasteranes and tetracyclic polyprenoids. For peak identifications refer to table 19. 154
Figure 101: Partial dendrogram of the hierarchical cluster analysis of Group 7 in Figure 70. 156
Figure 102: Partial *m/z* 191 mass chromatograms of representative degraded asphaltite (7666) in Group 7 showing the distribution of tricyclic terpanes and hopanes. For peak identifications refer to table 18. 157
Figure 103: Partial *m/z* 205 mass chromatograms of representative degraded asphaltite (7666) in Group 7 showing the distribution of methylhopanes. For peak identifications refer to table 18. 157
Figure 104: Partial *m/z* 217 mass chromatograms of representative degraded asphaltite (7666) in Group 7 showing the distribution of steranes and diasteranes. For peak identifications refer to table 19. 157
Figure 105: Partial *m/z* 259 mass chromatograms of representative degraded asphaltite (7666) in Group 7 showing the distribution of diasteranes and tetracyclic polyprenoids. For peak identifications refer to table 19. 158
Figure 106: Dendrogram of the hierarchical cluster analysis (HCA) of 29 source variables showing the relationship between asphaltite, waxy bitumen samples and FI oils. The groups are the same as those in Figure 70. 163
Figure 107: Partial dendrogram of the hierarchical cluster analysis of Group 6 in Figure 106 showing the relationship of Greenly-1 FI oil and the Group 6 samples. 164
Figure 108: Partial dendrogram of the hierarchical cluster analysis of Group 1 in Figure 106 showing the relationship of Gnarlyknots-1A FI oil and the Group 4 samples. 165
Figure 109: Representative chromatograms for asphaltite samples. (A) Whole-oil GC-MS TIC showing alkane distribution. (B) m/z 191 chromatogram showing distribution of terpanes. (C) m/z 217 chromatogram showing distribution of steranes and diasteranes. (D) m/z 218 chromatogram showing distribution of C27-C29 αββ steranes. (E) m/z 259 chromatogram showing distribution of C27-C29 βα diasteranes and TPP. For peak identifications refer to tables 18 and 19. 169
Figure 110: Representative chromatograms for Number 1 & 2 Rocks soft bitumen samples. (A) Whole-oil GC-MS TIC showing alkane distribution. (B) m/z 191 chromatogram showing distribution of terpanes. (C) m/z 217 chromatogram showing distribution of steranes and diasteranes. (D) m/z 218 chromatogram showing distribution of C27-C29 αββ steranes. (E) m/z 259 chromatogram showing distribution of C27-C29 βα diasteranes and TPP. For peak identifications refer to tables 18 and 19. 170
Figure 111: Representative chromatograms for Type I waxy bitumens. (A) Whole-oil GC-MS TIC showing alkane distribution. (B) m/z 191 chromatogram showing distribution of terpanes. (C) m/z 217 chromatogram showing distribution of steranes and diasteranes. (D) m/z 218 chromatogram showing distribution of C27-C29 αββ steranes. (E) m/z 259 chromatogram showing distribution of C27-C29 βα diasteranes and TPP. For peak identifications refer to tables 18 and 19. 172

Figure 112: Representative chromatograms for Type II waxy bitumen. (A) Whole-oil GC-MS TIC showing alkane distribution. (B) m/z 191 chromatogram showing distribution of terpanes. (C) m/z 217 chromatogram showing distribution of steranes and diasteranes. (D) m/z 218 chromatogram showing distribution of C27-C29 αββ steranes. (E) m/z 259 chromatogram showing distribution of C27-C29 βα diasteranes and TPP. For peak identifications refer to tables 18 and 19. 174
Figure 113: Representative chromatograms for Type IIIA waxy bitumen. (A) Whole-oil GC-MS TIC showing alkane distribution. (B) m/z 191 chromatogram showing distribution of terpanes. (C) m/z 217 chromatogram showing distribution of steranes and diasteranes. (D) m/z 218 chromatogram showing distribution of C27-C29 αββ steranes. (E) m/z 259 chromatogram showing distribution of C27-C29 βα diasteranes and TPP. For peak identifications refer to tables 18 and 19. 176
Figure 114: Representative chromatograms for Type IIIB waxy bitumen. (A) Whole-oil GC-MS TIC showing alkane distribution. (B) m/z 191 chromatogram showing distribution of terpanes. (C) m/z 217 chromatogram showing distribution of steranes and diasteranes. (D) m/z 218 chromatogram showing distribution of C27-C29 αββ steranes. (E) m/z 259 chromatogram showing distribution of C27-C29 βα diasteranes and TPP. For peak identifications refer to tables 18 and 19. 178
Figure 115: Representative chromatograms for Type IIIC waxy bitumen. (A) Whole-oil GC-MS TIC showing alkane distribution. (B) m/z 191 chromatogram showing distribution of terpanes. (C) m/z 217 chromatogram showing distribution of steranes and diasteranes. (D) m/z 218 chromatogram showing distribution of C27-C29 αββ steranes. (E) m/z 259 chromatogram showing distribution of C27-C29 βα diasteranes and TPP. For peak identifications refer to tables 18 and 19. 180
Figure 116: Representative chromatograms for Type IIID waxy bitumen. (A) Whole-oil GC-MS TIC showing alkane distribution. (B) m/z 191 chromatogram showing distribution of terpanes. (C) m/z 217 chromatogram showing distribution of steranes and diasteranes. (D) m/z 218 chromatogram showing distribution of C27-C29 αββ steranes. (E) m/z 259 chromatogram showing distribution of C27-C29 βα diasteranes and TPP. For peak identifications refer to tables 18 and 19. 182
Figure 117: Representative chromatograms for Type IIIE waxy bitumen. (A) Whole-oil GC-MS TIC showing alkane distribution. (B) m/z 191 chromatogram showing distribution of terpanes. (C) m/z 217 chromatogram showing distribution of steranes and diasteranes. (D) m/z 218 chromatogram showing distribution of C27-C29 αββ steranes. (E) m/z 259 chromatogram showing distribution of C27-C29 βα diasteranes and TPP. For peak identifications refer to tables 18 and 19. 184
Figure 118: Representative chromatograms for Type IVA waxy bitumen. (A) Whole-oil GC-MS TIC showing alkane distribution. (B) *m/z* 191 chromatogram showing distribution of terpanes. (C) *m/z* 217 chromatogram showing distribution of steranes and diasteranes. (D) *m/z* 218 chromatogram showing distribution of C_{27}-C_{29} αββ steranes. (E) *m/z* 259 chromatogram showing distribution of C_{27}-C_{29} βα diasteranes and TPP. For peak identifications refer to tables 18 and 19. 186
Figure 119: Representative chromatograms for Type IVB waxy bitumen. (A) Whole-oil GC-MS TIC showing alkane distribution. (B) m/z 191 chromatogram showing distribution of terpanes. (C) m/z 217 chromatogram showing distribution of steranes and diasteranes. (D) m/z 218 chromatogram showing distribution of C27-C29 αββ steranes. (E) m/z 259 chromatogram showing distribution of C27-C29 βα diasteranes and TPP. For peak identifications refer to tables 18 and 19. 188
Figure 120: Representative chromatograms for Type IVC waxy bitumen. (A) Whole-oil GC-MS TIC showing alkane distribution. (B) m/z 191 chromatogram showing distribution of terpanes. (C) m/z 217 chromatogram showing distribution of steranes and diasteranes. (D) m/z 218 chromatogram showing distribution of C27-C29 αββ steranes. (E) m/z 259 chromatogram showing distribution of C27-C29 βα diasteranes and TPP. For peak identifications refer to tables 18 and 19. 190

Figure 121: Representative chromatograms for Type IVD waxy bitumen. (A) Whole-oil GC-MS TIC showing alkane distribution. (B) m/z 191 chromatogram showing distribution of terpanes. (C) m/z 217 chromatogram showing distribution of steranes and diasteranes. (D) m/z 218 chromatogram showing distribution of C27-C29 αββ steranes. (E) m/z 259 chromatogram showing distribution of C27-C29 βα diasteranes and TPP. For peak identifications refer to tables 18 and 19. 192
Figure 122: Representative chromatograms for Type IVE waxy bitumen. (A) Whole-oil GC-MS TIC showing alkane distribution. (B) m/z 191 chromatogram showing distribution of terpanes. (C) m/z 217 chromatogram showing distribution of steranes and diasteranes. (D) m/z 218 chromatogram showing distribution of C27-C29 αββ steranes. (E) m/z 259 chromatogram showing distribution of C27-C29 βα diasteranes and TPP. For peak identifications refer to tables 18 and 19. 194
Figure 123: Representative chromatograms for Sandy River soft bitumen. (A) Whole-oil GC-MS TIC showing alkane distribution. (B) m/z 191 chromatogram showing distribution of terpanes. (C) m/z 217 chromatogram showing distribution of steranes and diasteranes. (D) m/z 218 chromatogram showing distribution of C27-C29 αββ steranes. (E) m/z 259 chromatogram showing distribution of C27-C29 βα diasteranes and TPP. For peak identifications refer to tables 18 and 19. 196
Figure 124: Hierarchical cluster analysis (HCA) of coastal bitumen samples. Left labels correspond to individual oil family assessment. 198
Figure 125: Carbon isotope signatures of coastal bitumens collected from southern Australian beaches prior to 1995 (after Edwards et al., 2016). 201
Figure 126: Map showing the location of the Indonesian basins sampled and the geographical distribution of their different oil types (after ten Haven & Schiefelbein, 1995). 203
Figure 127: Dendrogram showing hierachical clustering of 193 oils from 19 Indonesian sedimentary basins (after ten Haven & Schiefelbein, 1995). 204
Figure 128: Principal components analysis (PCA) of geochemical data on Indonesian oils (after ten Haven & Schiefelbein, 1995). The key discriminators are shown in panel A.................................... 205
Figure 129: Partial m/z 191 chromatograms of five representative Indonesian oil types (after ten Haven and Schiefelbein, 1995). 206
Figure 130: Dendrogram showing clustering of oils from Central and South Sumatra, and map illustrating the geographical distribution of different oil types (after ten Haven & Schiefelbein, 1995). 209
Figure 131: Map of selected sedimentary basins within the Indonesian Archipelago showing the locations of oil seeps and the pathways of the Indonesian and South China Sea throughflows (after Edwards et al., 2017 and references cited therein)... 210
Figure 132: Comparison of the biomarker signatures of Greenly-1 fluid inclusions and Type IIID waxy bitumen (sample W13/007499). Although HCA statistical treatment suggests that this waxy bitumen is comparable to the fluid inclusions from Greenly-1, there are clear differences in their respective alkane compositions which do not support their correlation to the same source. 212
Figure 133: Comparison of the biomarker signatures of Gnarlyknots-1A fluid inclusions and Type IVE waxy bitumen (sample W13/007881). Although some similarity exists, there are clear differences in their alkane compositions which do not support their correlation to the same source................... 213
Figure 134: Generalised timeframe for crude oil biodegradation modified after Head et al., (2006). Note that coastal bitumen occupies the right-hand third of this plot... 216
Figure 135: Summary of the Wenger et al., (2002) and Peters & Moldowan (1993) biodegradation scales. Figure modified after Head et al., (2003). Note that this is a generalised classification system subject to variation on a case-by-case basis.. 217

Figure 136: Asphaltites displaying characteristic conchoidal fractures. (A) Sample W13/007742, a typical asphaltite. (B) Sample W13/007664, a highly degraded asphaltite collected from Tractor Beach...219
Figure 137: Variation in whole-oil GC-MS chromatograms of asphaltites attributable to weathering. Each chromatogram is scaled such that no compound which is not a product of biodegradation may have a higher response than the freshest sample. Most of the asphaltites collected are comparable to the slightly biodegraded sample W13/007507. The unusually fresh (sample W13/007976) and highly weathered (sample W13/007566) specimens are rare exceptions. Sample W13/007664 is an example of the highly degraded asphaltite specimens found only at Tractor Beach. These highly degraded samples required analysis using a splitless injection (no dilution) in order to resolve the remaining hydrocarbons, which are present in extremely low abundance. 220
Figure 138: Asphaltites sub-sampled in cross-section to assess variability using CSIA. Sampled locations marked on each specimen (A) Sample W13/007507. (B) Sample W13/007742. (C) Sample W13/007976. (D) Sample W13/007672. 222
Figure 139: Difference in the carbon isotopic composition of individual *n*-alkanes of asphaltite sub-samples compared to the specimen interior. (A) Sample W13/007507. (B) Sample W13/007742. (C) Sample W13/007976. (D) Sample W13/007672..223
Figure 140: Assessment of sterane and diasteranes degradation in asphaltites. Each chromatogram is scaled such that no compound which is not a product of biodegradation may have a higher response than the freshest sample. Selected samples include the freshest asphaltite (W13/007976), a moderately biodegraded asphaltite (W13/007566) and a highly degraded asphaltite (W13/007663). (A)Sterane and diasteranes degradation identified in m/z 217. Co-eluting compounds are separated in later sections (B) Steranes (αββ) degradation identified in m/z 218. (C) Diasterane (βα) degradation identified in m/z 259. For peak identifications refer to table 19. 225
Figure 141: Assessment of the degradation of terpanes in asphaltites in the m/z 191 chromatogram. Each chromatogram is scaled such that no compound which is not a product of biodegradation may have a higher response than the freshest sample. Fresh to moderately degraded samples (W13/007976 and W13/007566) show minimal alteration of biomarkers. In heavily degraded examples such as W13/007664, many components are lost and others severely altered. For peak identifications refer to table 18. 226
Figure 142: Examples of surficial browning of waxy bitumen associated attributable to weathering: (A) Sample W13/007625 exhibiting partial browning. (B) Sample W13/007521, a highly degraded waxy bitumen with an entirely brown and brittle exterior. (C) Sample W13/007521 in cross-section, highlighting that browning is restricted to its exposed exterior. 227
Figure 143: Example of GC-MS whole-oil degradation assessment using exterior vs. interior analysis. (A) Whole-oil GC-MS chromatogram of the exterior of extremely degraded Type I waxy bitumen W13/007521. (B) Whole-oil GC-MS chromatogram of the interior of sample W13/007521. (C) Whole-oil GC-MS chromatogram of the freshest example of the Type I waxy bitumen (W13/007601).......228
Figure 144: Degradation overview for Type I waxy bitumen (high botryococcane). Each chromatogram is scaled such that no compound which is not a product of biodegradation may have a higher response than the freshest sample. (A) Representative examples of degradation states revealed by whole-oil GC-MS analysis. (B) Histogram plot of the lightest preserved *n*-alkane from each beach survey...230
Figure 145: Historical continuity of Type I waxy bitumen stranding: (A) Sample 4066 collected in 1961 and analysed by Padley (1995). (B) Sample 28 collected in 1990 and analysed by Padley (1995). (C)

Sample W13/007601 collected in 2015 during the second coastal survey of the GABRP. This specimen is the freshest example of Type I waxy bitumen collected between 2014 and 2016. Abbreviations: Np = norpristane, Pr = pristane, Ph = phytane, B = botryococcane, IS = internal standard of 3-methylheneicosane used by Padley (1995), numbers = *n*-alkane chain lengths. 231
Figure 146: Degradation overview for Type II waxy bitumen (low botryococcane). Each chromatogram is scaled such that no compound which is not a product of biodegradation may have a higher response than the freshest sample. (A) Representative examples of degradation states revealed by whole-oil GC-MS analysis. (B) Histogram plots of the lightest preserved n-alkane from each beach survey. 232
Figure 147: Historical continuity of Type II waxy bitumen stranding. Each chromatogram is scaled such that no compound which is not a product of biodegradation may have a higher response than the freshest sample. (A) Sample A923.99 collected in 1983 and subsequently analysed by Padley (1995). (B) Sample 12 collected in 1990 and analysed by Padley (1995). (C) Sample W13/007615 collected in 2015 during the second survey of the GABRP. This specimen is the freshest example of type II waxy bitumen collected between 2014 and 2016. Abbreviations: Np = norpristane, Pr = pristane, Ph = phytane, B = botryococcane, IS = internal standard of 3-methylheneicosane used by Padley (1995), numbers = *n*-alkane chain lengths. 233
Figure 148: Degradation overview for Type III waxy bitumen (no botryococcane, low wax). Each chromatogram is scaled such that no compound which is not a product of biodegradation may have a higher response than the freshest sample. (A) Representative examples of degradation states revealed by whole-oil GC-MS analysis. (B) Histogram plots of lightest preserved *n*-alkane from each annual survey. 235
Figure 149: Degradation overview for Type IV waxy bitumen (no botryococcane, high wax). Each chromatogram is scaled such that no compound which is not a product of biodegradation may have a higher response than the freshest sample. (A) Range of degradation states revealed by whole-oil GC-MS analysis. (B) Histogram plots of their lightest preserved *n*-alkane from each annual survey. 237
Figure 150: Summary of sterane and diasterane degradation in Type I waxy bitumen from the freshest identified sample (W13/007601) to a highly degraded sample (W13/007737). Each chromatogram is scaled such that no compound which is not a product of biodegradation may have a higher response than the freshest sample. (A) Sterane and diasteranes degradation observed in *m/z* 217 chromatogram. (B) Degradation of C_{27}-C_{29} αββ steranes observed in the *m/z* 218 chromatogram. (C) Degradation of C_{27}-C_{29} βα diasteranes observed in the *m/z* 259 chromatogram. For peak identifications refer to table 19. 239
Figure 151: Summary of terpane degradation in Type I waxy bitumen from the freshest identified sample (W13/007601) to a highly degraded sample (W13/007737) using the *m/z* 191 chromatogram. Each chromatogram is scaled such that no compound which is not a product of biodegradation may have a higher response than the freshest sample. For peak identifications refer to table 19. 240
Figure 152: Mean sea level pressure (M.S.L.P units hPa) for Australia on 26th January 2012. Winds for the SA region are directed to the northwest. 244
Figure 153: February average of wind stress obtained (after Trenberth et al., 1989). The vector indicated has a magnitude of 0.1 Pa and the contours of wind stress with magnitudes of 0.025 Pa and 0.05 Pa are indicated, (from Middleton & Platov, 2003). 245
Figure 154: Average winds measured by coastal weather station for January-February-March 2014. 245

Figure 155: M.S.L.P. (units hPa) for Australia for the 22nd September 2011. Winds for the SA region are directed to the east. 246
Figure 156: Wind mean wind stress field for winter. A legend vector of 0.05 Pa is indicated (Middleton and Cirano, 2002). 247
Figure 157: Average winds measured by coastal weather station for July-August-September 2014. 247
Figure 158: Upper Panel: A schematic of some key circulation features for winter, including the Leeuwin Current (LC), Leeuwin Under-Current (LUC), Flinders Current (FC), shelf-edge South Australian Current (SAC) and coastal currents (CC). Water is downwelled throughout and a dense salty outflow from the Gulfs. Lower Panel: Summertime circulation and upwelling occurs off Kangaroo Is and the Bonney Coast. Shelf edge downwelling may occur in the western Bight........ 249
Figure 159: An SST image for August 2011. Warm water associated with the Leeuwin Current enters the western GAB: temperature scale shown. Surface sea level height (altimeter data) is indicated by the white contours. The surface geostrophic velocities are also shown with a legend arrow of 0.5 m/s. The magenta arrow heads denote surface drifter positions at 12h intervals. The cyan line denotes the 200 m isobath and shelf edge. (Source: oceancurrent.imos.org.au). 250
Figure 160: A SST image for 28th January 2012. Warm (23 °C) water associated with heating in the shallow Gulfs is shown along with cold (14-18 °C) upwelled water off the Bonney Coast, Kangaroo Island and the Eyre Peninsula: temperature scale shown. Surface sea level height (altimeter data) is indicated by the white contours. The surface geostrophic velocities are also shown with a legend arrow of 0.5 m/s. The magenta lines correspond to HF RADAR daily-averaged currents with a legend arrow of 0.5 m/s shown. The magenta arrows denote surface drifter positions. The cyan line denotes the 200 m isobath and shelf edge. (Source oceancurrent.imos.org.au). 251
Figure 161: Climatological 90th percentile wave height (see key) and direction (arrow heads) for February (upper panel) and September (lower panel), from Hemer & Griffin (2010). For other months and percentiles, see http://www.marine.csiro.au/~griffin/ORE/wave_height/index.html.. 253
Figure 162: The ROMS model domain ("SAM") used in this study. The 100 m, 200 m and 1400 m isobaths are shown. The mooring locations of SAM5CB (Coffin Bay), NRSKAI (Kangaroo island), SAM7DS (deep 600 m mooring) and the BP moorings BPM1 (shelf edge) and BPM2 (shelf slope) are shown. The thick straight black line indicates the repeat SAIMOS CTD line. The red lines denote the location of cross-sectional (seasonal averaged) model results. The green boxes denote the domains for which all available temperature data is obtained so as to compare with the (red line) cross section model results. The number N of temperature data casts for each green box is indicated for summer and winter. 257
Figure 163: As in Figure 162 but for the BRAN2015 model domain used by CSIRO in this study. The thin blue line demarcates the model open boundary. 257
Figure 164: Asphaltite and tarball potential offshore seeding locations used in oceanographic forward models. 261
Figure 165: Beach locations used as seeding locations for backtrack models. 263
Figure 166: ROMs winter and summer offshore seeded particle trajectories using currents only for 2011. 265
Figure 167: ROMs winter and summer offshore seeded particle trajectories using currents only for 2012. 266
Figure 168: ROMs winter and summer offshore seeded particle trajectories using currents only for 2013. 267

Figure 169: ROMs winter and summer offshore seeded particle trajectories using currents only for 2014. 268
Figure 170: BRAN2015 three-monthly offshore seeded particle trajectories combining surface currents and Stokes drift for 2014. 271
Figure 171: BRAN2015 three-monthly offshore seeded particle trajectories combining surface currents and Stokes drift for 2015. 272
Figure 172: BRAN2015 three-monthly offshore seeded particle trajectories combining surface currents and Stokes drift for 2016. 273
Figure 173: BRAN2015 two-monthly offshore seeded particle trajectories combining surface currents and Stokes drift for 2014. 275
Figure 174: BRAN2015 two-monthly offshore seeded particle trajectories combining surface currents and Stokes drift for 2015. 276
Figure 175: BRAN2015 two-monthly offshore seeded particle trajectories combining surface currents and Stokes drift for 2016. 277
Figure 176: Heat map showing cumulative offshore seeded particles location for 2011–2016 April-September using BRAN2015. 278
Figure 177: Heat map showing cumulative offshore seeded particles locations for 2011–2011 October-March using BRAN2015. 278
Figure 178: BRAN2015 three-monthly backtrack particle trajectories combining surface currents and Stokes drift for 2014. 281
Figure 179: BRAN2015 three-monthly backtrack particle trajectories combining surface currents and Stokes drift for 2015. 282
Figure 180: BRAN2015 three-monthly backtrack particle trajectories combining surface currents and Stokes drift for 2016. 283
Figure 181: Heat map showing cumulative offshore seeded particles location for 2014–2016 April–September using BRAN2015. 285
Figure 182: Heat map showing cumulative offshore seeded particles locations for 2014–2011 October–March using BRAN2015. 285
Figure 183: Key observations from oceanographic forward and backtrack models incorporating Stokes drift. 287
Figure 184. Example 2D seismic line (DH91-227) from SW-NE showing typical fluid escape features. 287
Figure 185: ROMS model (70-day duration) of seafloor release of neutrally buoyant particles (John Middleton, pers comm.). 289
Figure 186 BRAN2015 three monthly offshore seeded particle trajectories combining surface currents and stokes drift for 2011. 315
Figure 187 BRAN2015 three monthly offshore seeded particle trajectories combining surface currents and stokes drift for 2012. 316
Figure 188 BRAN2015 three monthly offshore seeded particle trajectories combining surface currents and stokes drift for 2013. 317
Figure 189. BRAN2015 three monthly back track particle trajectories combining surface currents and stokes drift for 2011. 318
Figure 190. BRAN2015 three monthly back track particle trajectories combining surface currents and stokes drift for 2012. 318

Figure 191. BRAN2015 three monthly back track particle trajectories combining surface currents and stokes drift for 2013. 318
Figure 192. BRAN2015 two monthly offshore seeded particle trajectories combining surface currents and stokes drift for 2011. 319
Figure 193. BRAN2015 two monthly offshore seeded particle trajectories combining surface currents and stokes drift for 2012. 320
Figure 194. BRAN2015 two monthly offshore seeded particle trajectories combining surface currents and stokes drift for 2013. 321

LIST OF TABLES

Table 1: Hydrocarbon indications and shows. 15
Table 2: South Australian beaches monitored in detail for the stranding of coastal bitumen during the 1990-1991 Coastal Bitumen Survey. 38
Table 3: Beaches visited 2014. 42
Table 4: Beaches visited in 2015. 43
Table 5: Beaches visited in 2016. 45
Table 6: Classes of debris type, colour and size used to log debris encountered. 51
Table 7: Number of pieces per 100m surveyed for hard plastic and plastic rope debris. 52
Table 8: Sample numbers collected per bitumen type and year. 54
Table 9: Cummulative total sample numbers by bitumen family for each beach visted. 55
Table 10: Sample numbers collected on the beaches by bitumen type for each year. 57
Table 11: Summary of analytical procedures. Any data still being collected (in progress) is not included or discussed in this report. 90
Table 12: Tabulated summary of samples collected for each beach. 91
Table 13: Targeted compounds in whole oil GC-MS geochemistry screening (split). Retention times are listed in minutes. Nd = not done (not present to identify or outside analytical range). Target ions for specific compounds were as follows: n-alkanes = 57; pristane = 57 + 183; phytane = 57 + 197; botryococcane = 57 + 294. 93
Table 14: Target compounds in m/z 217, 218, 259 (steranes). Note retention times for biomarkers varied by ± 1 minute required manual integration for all samples. 98
Table 15: Target compounds in m/z 191 (terpanes). Note that retention times for biomarkers varied by ± 1 minute. 99
Table 16: Summary of target compounds for MRM analysis. TT = tricyclic terpanes; Tet = tetracyclic terpanes. Channel ranges for each compound are given. 101
Table 17: Summary of selected biomarkers and their related source indicators. 118
Table 18: Peak assignments for terpanes in the *m/z* 191 and 205 mass chromatograms. 120
Table 19: Peak assignments for steranes, diasteranes and methylsteranes in the *m/z* 217 and 259 mass chromatograms and MRM chromatograms. 121
Table 20: Summary of potential source rocks of the Group 1, 2 3 bitumens and their biomarker indicators. 158
Table 21: Summary of potential source rocks of the Group 4 and 5 bitumens and their biomarker indicators. 159

Table 22: Summary of potential source rocks of the Group 6 and 7 bitumens and their biomarker indicators. 160
Table 23: Summary of key source-related biomarker indicators (after Peters et al., 2005) 166
Table 24: Summary of source characteristics and key features of asphaltites and Number 1 & 2 Rocks soft bitumen. 167
Table 25: Summary of source characteristics and key features of Type I waxy bitumens. 171
Table 26: Summary of source characteristics and key features of Type II waxy bitumens. 173
Table 27: Summary of source characteristics and key features of Type IIIA waxy bitumens. 175
Table 28: Summary of source characteristics and key features of Type IIIB waxy bitumens. 177
Table 29: Summary of source characteristics and key features of Type IIIC waxy bitumens. 179
Table 30: Summary of source characteristics and key features of Type IIID waxy bitumens. 181
Table 31: Summary of source characteristics and key features of Type IIIE waxy bitumens. 183
Table 32: Summary of source characteristics and key features of Type IVA waxy bitumen. 185
Table 33: Summary of source characteristics and key features of Type IVB waxy bitumens. 187
Table 34: Summary of source characteristics and key features of Type IVC waxy bitumen. 189
Table 35: Summary of source characteristics and key features of Type IVD waxy bitumens. 191
Table 36: Summary of source characteristics and key features of Type IVE waxy bitumens. 193
Table 37: Summary of source characteristics and key features of Sandy River soft bitumens. 195
Table 38: Diagnostic characteristics and source affinity of waxy bitumens collected from ocean beaches in South Australia and western Victoria prior to 1995 (after Edwards et al., 2017). 199
Table 39: Key biomarker characteristics of West Indonesian oil families, their locations and their likely source affinities (after Edwards et al., 2017). 202
Table 40: Typical values of the south-easterly components of the mean and standard deviation (S. Dev.) of the wind stress: units Pascals. The similar statistic is presented in brackets but for the corresponding wind speed in m/s: 10 m/s = 36 km/hr. A positive mean is directed to the south-east along the shelf. The maximum wind stress most likely to be experienced in any year is also given and was inferred from Trenberth et al., (1989). The heat fluxes are from the NCAR/NCEP (Kalnay et al., 1996) climatology for the GAB while those in brackets are for the Head of the Bight (Herzfeld, 1997). 246
Table 41: Wave climatology for the mid-Bight as inferred from Caires et al., (2005) including the significant wave height HS, period T, phase speed c, wavelength λ. The surface and bottom water velocities are denoted by Uo and Ub the (Stokes) drift velocity by Ud. The standard deviations (σ) of HS and T are also presented: units metres. Note the significant wave height is the average height of the top 33% of wave maxima averaged over a month. 254
Table 42: Parameters and forcing components used for the ROMS and BRAN models in the study. The acronyms, abbreviations and references used are indicated below. 257
Table 43: Offshore seeding locations for the forward track oceanographic models. 260
Table 44: Beaches used as seeding locations for backtrack models. 262

ACKNOWLEDGEMENTS

This project was funded through the Great Australian Bight Research Program, a collaboration between BP, CSIRO, SARDI, the University of Adelaide and Flinders University.

The authors of this report would like to thank Dianne Edwards for her support of the project through the provision of prior data sets and valuable insights which were shared with the project team throughout the duration of this project. Members of the South Australian Geological Survey and in particular Les Tucker and Sue Margot are thanked for their assistance in compiling historical datasets and providing details about survey beaches. Stuart Valladares is thanked for his donation of a large number of samples collected from Avoid Bay, as are all of the other members of the public who donated samples to the project. Mark Rollog and Robyn Williamson at the University of Adelaide are thanked for their analytical and preparatory assistance with IRMS & EA analyses. Staff at CSIRO, the University of Adelaide and BP are thanked for their support in the development and execution of this project, as are the project team at SARDI (Jane Ham, Ben Baghurst and Steven Lapidge).

EXECUTIVE SUMMARY

This report contains the results of the first multi-annual geospatial, geochemical and oceanographic study of the stranding of coastal bitumen (asphaltite and tar balls) on representative ocean beaches (n = 31) along the entire coastline of South Australia. Previous investigations of this phenomenon, dating back to the mid-1800s, were episodic and limited to beaches on the Limestone Coast, southern Kangaroo Island and the foot of Eyre Peninsula. The present study revisited the same 31 beaches after winter in 2014, 2015 and 2016, collecting a total of 631 specimens, and in so doing filled a major gap in our knowledge of bitumen stranding along the western side of Eyre Peninsula to the head of the Great Australian Bight.

This investigation employed an updated version of the NOAA SCAT method for assessing shoreline oiling conditions in order to establish the natural baseline hydrocarbon loading of the South Australian coastline. Major findings from this part of the project are:

- Tar balls (waxy bitumen) preferentially strand in the upper intertidal to upper shore zones of southwest-facing ocean beaches, whereas the less common, denser asphaltites tend to accumulate on beaches with a northwest aspect.
- The number and size of individual strandings is considerably less than reported for the period 1960-1995.
- Waxy bitumens strand along the entire South Australian shoreline, with a particular focus on the Limestone Coast.
- Asphaltites are more commonly found along the west coast of Eyre Peninsula, suggesting different transport mechanisms and/or a different point of origin.
- The high abundance of waxy bitumens with geochemical similarities to Indonesian-sourced oils is consistent with the transport of these materials as flotsam, first in the southward Leeuwin Current which then feeds into the eastward-flowing coastal and South Australian currents.

The resulting catalogued collection of asphaltites and tar balls, the largest yet assembled for any geochemical investigation of this type in Australia, underwent detailed physical, elemental, isotopic and biomarker characterisation. The principal findings of this work are:

- Fifteen oil families and sub-families of South Australian coastal bitumen were identified, significantly more than the six families known from previous studies.
- The waxy bitumens differ from those found along the same coastline between 1960 and 1995 in being much more weathered and biodegraded, consistent with both their smaller size and lesser numbers.
- Soft asphaltic bitumen recovered from a site on the Limestone Coast is unique, and likely represents an early expulsion product from a Cretaceous marine source rock similar to that which gave rise to the asphaltites. Both point to the likely existence of an active petroleum system in the Bight Basin.
- The majority of the waxy bitumens have distinctive Cenozoic lacustrine biomarker signatures which mark their origin from distant offshore oil seeps in the Indonesian Archipelago.
- The abundance of both asphaltite and waxy bitumen stranding on South Australian beaches has declined dramatically over the past 20+ years, attesting to a diminution of seep activity

and/or, in the case of the latter, improved environmental practices related to tanker washing and oil spillage within Indonesian waters.

- At least two waxy bitumen sub-families lack Indonesian signatures and could therefore originate from seeps in offshore basins along Australia's western and southern continental margin.
- The discovery of several new oil families of non- Indonesian provenance among the ocean wanderer bitumens that impact the South Australian coastline has potentially important implications for the prospectivity of its offshore sedimentary basins.

For the first time oceanographic modelling was employed to develop an understanding of the transport of coastal bitumens in the Great Austalian Bight (GAB). The findings show that:

- Oceanographic models which simulate currents alone do not adequately account for the observed stranding locations of tarballs and asphaltite.
- Models which simulate both currents and Stokes drift can describe their stranding locations across the region.
- Winter strandings are dominated by materials transported from west to east by the Leeuwin Current and storms.
- The winter modelled conditions can supply materials to all of the beaches in the GAB from areas along the shelf break at the western extent of the model, consistent with the discovery of Indonesian-sourced waxy bitumens on all the beaches surveyed.
- The winter modelling shows that there is a low probability of bitumens sourced in the Ceduna or Duntroon sub-basins reaching the coastline at the Head of the Bight and on the northern Eyre Peninsula.
- Summer strandings are dominated by materials transported from the southeast by Stokes drift caused by strong northerly to northwesterly winds.
- Throughout all seasons there is a low probability of any materials sourced in the Morum sub-basin travelling to the west of Kangaroo Island and encountering the ocean beaches on Eyre Peninsula.
- The area with the highest frequency of particle tracks is located to the west of Kangaroo Island and overlies the Duntroon sub-basin and the eastern part of the Ceduna sub-basin.
- Any locally derived materials within this area can reach all beaches in the study area and there is seismic support for potential leakage indicators in this area.

These research findings have addressed and exceeded the original project objectives and offer an unprecedented insight into the transport mechanisms, stranding processes, alteration and source of coastal bitumens which are stranded along the coastlines of South Australia. The data produced forms an important, and continuing, baseline for hydrocarbon loadings on the beaches of South Australia and whilst a definitive origin of the new tarball oil families and asphaltites has not been established they provide evidence of active hitherto unknown regional petroleum systems.

Part I Introduction

INTRODUCTION

Overview

BP Developments Australia, CSIRO, the South Australian Research and Development Institute (SARDI), the University of Adelaide and Flinders University are working on a 4 year, $20 million research program to improve the understanding of the environmental, economic and social value of the Great Australian Bight (GAB). The GAB Research Program is administered by a Management Committee with representation from BP, CSIRO, SARDI, Adelaide University and Flinders University and is advised by an independent Science Panel (ISP) comprising internationally recognised experts in key discipline areas.

The GAB Research Program comprises 7 themes and 16 research projects. This report presents the findings of research conducted for Theme 5 (Petroleum Geology & Geochemistry) and Project 5.2 (Asphaltite and tarball surveys).

Background and need

The Great Australian Bight (GAB), and particularly the Ceduna Sub-basin, is considered one of the most prospective deepwater frontier basins in offshore Australia (Totterdell et al*.,* 2008). It contains up to 15 km of mid to late Cretaceous deltaic and marine sediments within the Tiger and Hammerhead Supersequences that provide potential reservoirs, seals and oil-prone source rocks at several stratigraphic levels (Blevin et al., 2000; Totterdell et al., 2000; Struckmeyer et al., 2001).

At the start of the Great Australian Bight Research Program (GABRP) no liquid hydrocarbons had been directly measured in the GAB and therefore no active petroleum system was proven. This was despite the determination of possible hydrocarbon migration routes and accumulation zones within some of the few exploration wells drilled in the basin (i.e. the detection of oil inclusions at low abundance) and indications that there are hydrocarbons naturally leaking into the GAB (i.e. asphaltite strandings).

Previous geochemical studies of the occurrence of coastal bitumens (McKirdy et al., 1986, 1994; Currie et al., 1992; Padley et al., 1993; Padley, 1995) have shown that the vast majority of the tarballs found are waxy bitumens which originated in the Indonesian Archipelago and were subsequently carried into South Australian waters by the South Equatorial and Leeuwin Currents. Notwithstanding their extra-GAB provenance, they are the dominant contributor to the natural hydrocarbon loading of southern Australia's coastline (Edwards et al., 2016). Moreover, as surface drifters (specific gravity 13–40° API) their stranding pattern provides a predictive template for the ultimate destination of any oil spill that might arise from exploration or production operations in the GAB.

The asphaltites are almost certainly of local origin, although the exact location of their parent petroleum system has yet to be established (Edwards et al., 1998, 1999; Totterdell et al., 2008; Hall et al., 2014). Their quasi-neutral buoyancy (4–18° API) implies that they were submerged or even bottom drifters. Hence, it is not surprising that their historical stranding pattern should differ markedly from that of the pelagic tarballs (see Padley, 1995; Edwards et al., 2016).

A detailed inventory of the different varieties of petroleum hydrocarbons (oil slicks, tarballs, asphaltites) known to strand along the adjacent South Australian coastline is required in order to 1) identify those most likely to originate from offshore hydrocarbon seeps, and 2) provide a baseline understanding of the nature and abundance of asphaltites and tarballs on the coastline before any major exploration or production of oil/gas commences in the Bight.

Objectives

In order to better constrain the provenance of coastal bitumen in the Great Australian Bight (GAB) region, Project 5.2 of the GABRP aimed to address key knowledge gaps identified within the literature:

1. The contemporary natural hydrocarbon loading of the South Australian coastline.

2. The sites of most frequent present-day (as opposed to historical) stranding of asphaltite and tarballs, and their geographic relationship to offshore sea surface currents.

3. Molecular and isotopic characteristics of a statistically significant population of freshly stranded asphaltites, necessary to determine their degree of weathering and hence their likely proximity to the parent seep(s).

To address these knowledge gaps Project 5.2 objectives were to:

1. Map and quantify the contemporary natural hydrocarbon loading of selected ocean beaches on Eyre Peninsula, Kangaroo Island and the Limestone Coast. The latter two areas being known sites for the regular stranding of asphaltites, waxy bitumens (tarballs) and/or oil slicks. The collection of tarballs and asphaltites on the beaches of South Australia will allow their geochemistry to be documented, and ascertain their probable origins using oceanographic and geological models.

Establishing the present-day hydrocarbon loading of the South Australian coastline (its geographic distribution, concentration in kg/km, compositional heterogeneity and principal sources) will act as a baseline against which the environmental impact of any spillage arising from future drilling operations in the GAB can be measured, and also serve as a predictive template for the likely destination(s) of such accidental spillage.

2. Identify the provenance and weathering of the asphaltites and any non-Indonesian tarballs and oil slicks using their elemental, isotopic and molecular fingerprints. In particular, their source and maturity-specific parameters will provide essential clues to their origin. These data, in combination with stranding distributions (GABRP Project 5.2 Objective 1); oceanographic modelling using a detailed knowledge of both the sea surface currents traversing the continental margin of South Australia, including zones of upwelling (Oceanography Theme); geological interpretations of leakage indicators and offshore seepage studies (Seeps and Leakage GABRP Project 5.1); and other petroleum migration, timing and accumulation indicators (Fluid Inclusions GABRP Project 5.3), will help delineate possible seafloor hydrocarbon leakage points within the GAB.

REGIONAL GEOLOGY OF THE BIGHT BASIN

The Bight Basin formed during the break-up of eastern Gondwana in the Late Jurassic–Early Cretaceous. It extends for ~2000 km along the Australian southern margin and comprises a series of extensional depocentres in modern day water depths between 200 m and >4000 m. No significant hydrocarbons have been found in the basin, which remains an exploration frontier.

Basin Outline

The Bight Basin is a large, mainly offshore basin situated along the western and central parts of the continental margin of southern Australia (Figure 1). The basin extends from the Leeuwin Fracture Zone in the west, to just south of Kangaroo Island in the east, where it adjoins the Otway Basin. The basin contains a number of depocentres that were formed by the rifting and thinning of the Australian Plate; including the Ceduna, Duntroon, Eyre, Bremer and Recherche sub-basins (Figure 1). The current sub-divisions of the Bight Basin are based on those defined by Bradshaw et al., (2003) and Totterdell & Bradshaw (2004) and have evolved from many previous basin definitions published by various researchers. Within the revised definition of the Bight Basin, the former Duntroon Basin has been remapped as a smaller, genetically related rift system along the margin of the main rift basin, and has been reclassified as a sub-basin. The Bight Basin is overlain unconfomably by dominantly cool-water carbonates of the Cenozoic Eucla Basin (Messent, 1996; Feary & James, 1998).

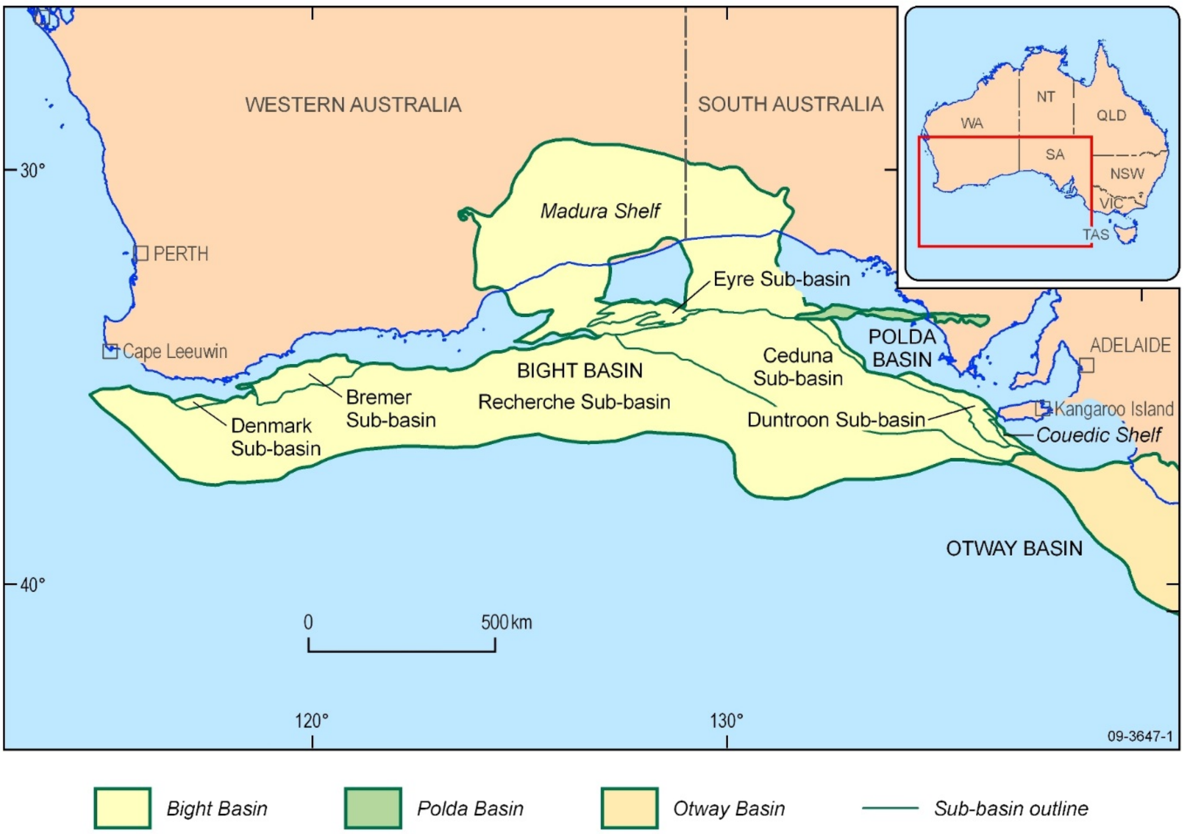

Figure 1: Location of the Bight Basin with component sub-basins. © Commonwealth of Australia (Geoscience Australia) 2016.

Basin evolution and tectonostratigraphic framework

The Bight Basin is a large Mesozoic to Cenozoic depocentre, which formed during the breakup of Gondwana (Fraser & Tilbury, 1979; Bein & Taylor, 1981; Willcox & Stagg, 1990; Hill, 1995; Totterdell et al. 2000; Norvick & Smith, 2011; Teasdale et al., 2003). The basin developed along Australia's southern margin during a period of extension and passive margin evolution that commenced in the Middle–Late Jurassic (Teasdale, 2003). The Ceduna Sub-basin, which is the focus of current hydrocarbon exploration activities, contains in excess of 15 km of syn- and post-rift Mesozoic sediments (Figure 2-4). It occurs in water depth ranging from 200 m to over 4000 m and has an area of approximately 90,000 km^2 (Sommerville, 2001). The northern margin is characterised by a series of fault-bound half grabens that contain Middle Jurassic to Early Cretaceous syn-rift fill (Figure 4). The southwestern boundary is interpreted at the basinward edge of an associated toe-thrust zone. The sub-basin is characterised by five main phases of evolution (King & Mee, 2004; Totterdell & Bradshaw, 2004; Blevin & Cathro, 2008):

- A Late Jurassic Early Cretaceous mechanical subsidence phase due to a phase of intracontinental extension. Extensional deformation in the Ceduna Sub-basin appears to have been focused along a pre-existing NW–SE-trending margin of the Gawler Craton resulted in simple half graben along the eastern margin of the sub-basin. The rift fill comprises the Callovian–Kimmeridgian Sea Lion Supersequence and the Tithonian–early Berriasian Minke Supersequence (Figure 5).
- An Early Cretaceous phase of slow thermal subsidence represented by the largely non-marine Berriasian Southern Right Supersequence and the Valanginian to mid-Albian Bronze Whaler Supersequence (Figure 5). The onlapping, sag-fill geometry of the succession suggests that accommodation was created largely by thermal subsidence and compaction, with deposition concentrated over the earlier half graben.
- A second period of active extension during the Early–Late Cretaceous causing rapid subsidence in the sub-basin. The high subsidence rates recorded from the mid-Albian were possibly controlled by an interplay between thermal subsidence, mechanical extension and gravity-driven growth faulting (Mulgara Fault Family) in the White Pointer delta. This period of accelerated subsidence continued until the commencement of sea-floor spreading between Australia and Antarctica in the Late Santonian, and coincided with a period of rising global sea level. This resulted in a major marine flooding event, and widespread deposition of the marine Blue Whale Supersequence, followed by deposition of the White Pointer and Tiger supersequences (Figure 5). Gravity-driven, detached extensional and contractional faults formed during the Cenomanian as a result of deltaic progradation. The deposition of the Tiger Supersequence coincides with a period of upper crustal extension resulting in the formation of large displacement, almost west–east-striking faults and the reactivation of many Cenomanian growth faults.
- The Late Cretaceous break-up associated with the first true oceanic crust at ~83 Ma (Sayers et al., 2001). This coincides with the base of the Hammerhead Supersequence (Figure 5). This boundary can be strongly erosional and characterised by significant incisions believed to be the result of uplift related to the commencement of sea-floor spreading.
- A post break-up thermal subsidence phase that coincided with the second, large progradational delta development resulting from a massive influx of sediments giving rise to the characteristic, prograding shelf-margin geometries of the Ceduna Delta succession with

the deposition of the Hammerhead Supersequence (Figure 5). A localised region of gravity-driven structures and simple, planar normal faulting developed with the latter reactivating older faults. Faulting appears to be latest Maastrichtian–Early Paleocene in age. Totterdell and Bradshaw (2004) suggest that the faulting was probably related to flexure of the margin caused by sediment loading during the Late Cretaceous.

Half-spreading rates were extremely slow from the Campanian (~83 Ma) until the Middle Eocene (~43 Ma), reaching a maximum of around 10 mm/year, although spreading rates were generally much less. From around 43 Ma, half-spreading rates rapidly increased to about 20 mm/year in a N-S orientation (Tikku & Cande, 1999). In the post Eocene period, deposition of marine carbonates reflects deepening water and the end of the effect of regional tectonics on the development of the Bight Basin (Fraser and Tilbury, 1979).

Late Cretaceous and Tertiary igneous rocks have been interpreted on seismic data (Totterdell et al., 2000) and Tertiary volcanic rocks have been dredged from the Bight Basin (Davies et al., 1989; Clarke & Alley, 1993). Schofield & Totterdell (2008) detailed the distribution of the volcanic and intrusive bodies in the Ceduna Sub-basin and related them to the acceleration in seafloor spreading during the Middle Eocene.

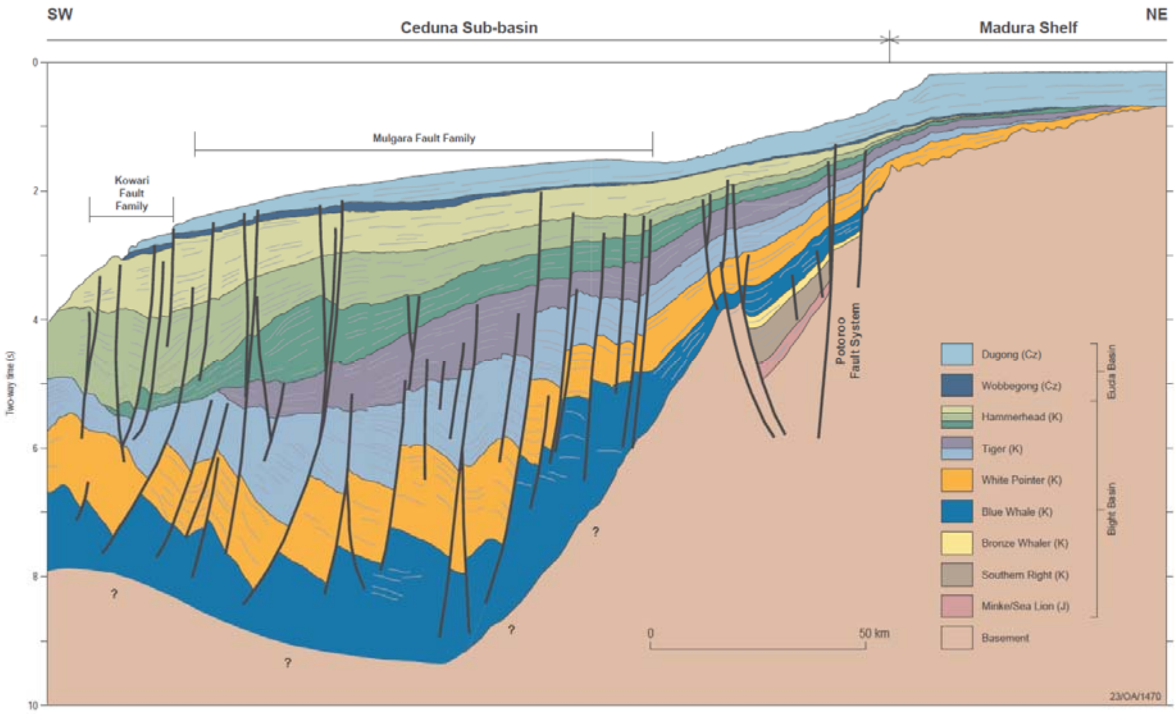

Figure 2: Cross-section through the eastern Madura Shelf and Ceduna Sub-basin. From Bradshaw et al., 2003.

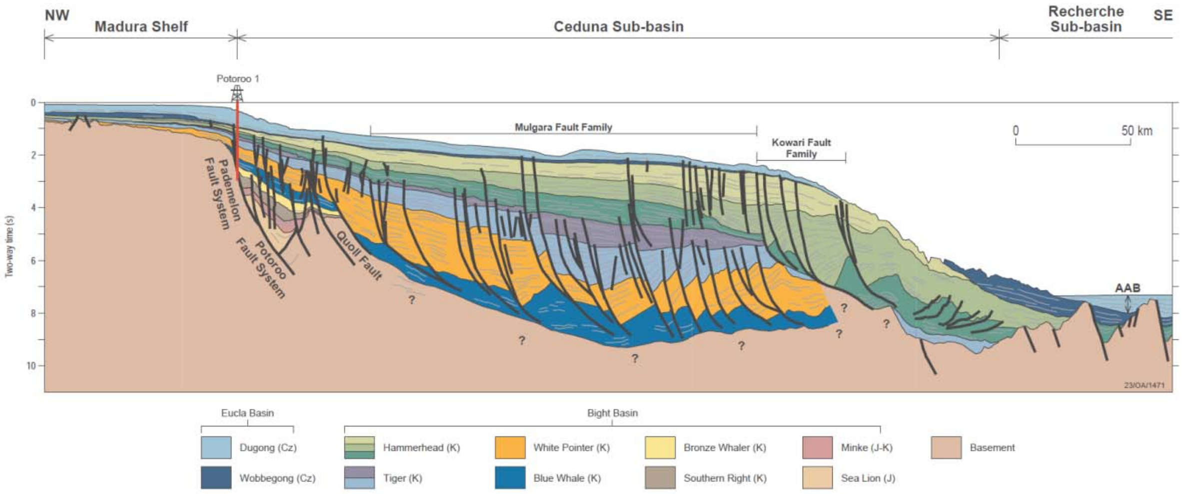

Figure 3: Cross-section through the eastern Madura Shelf, Ceduna Sub-basin and eastern Recherche Sub-basin. From Bradshaw et al., 2003.

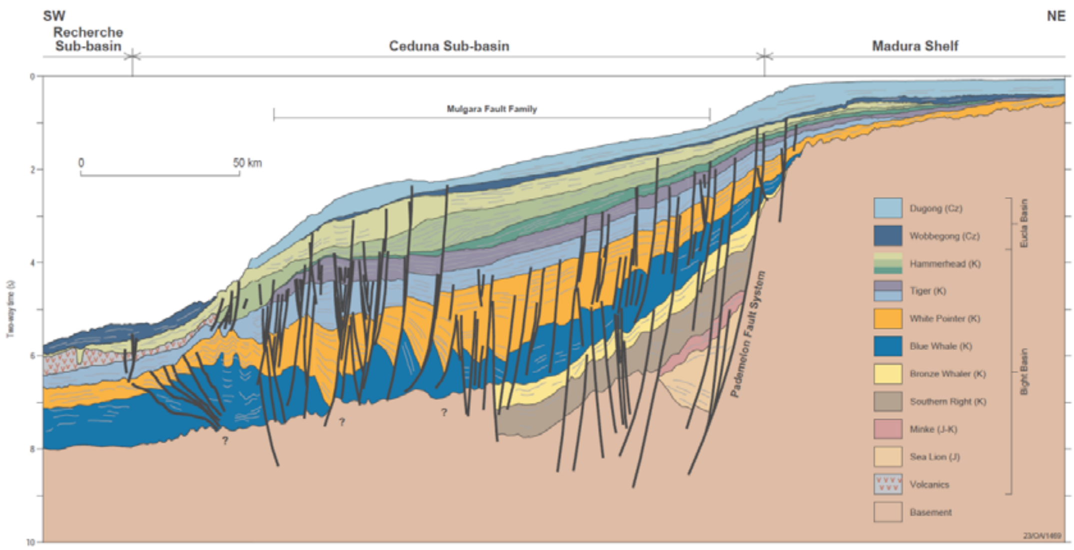

Figure 4: Cross-section through the eastern Madura Shelf, Ceduna Sub-basin and eastern Recherche Sub-basin. From Bradshaw et al., 2003.

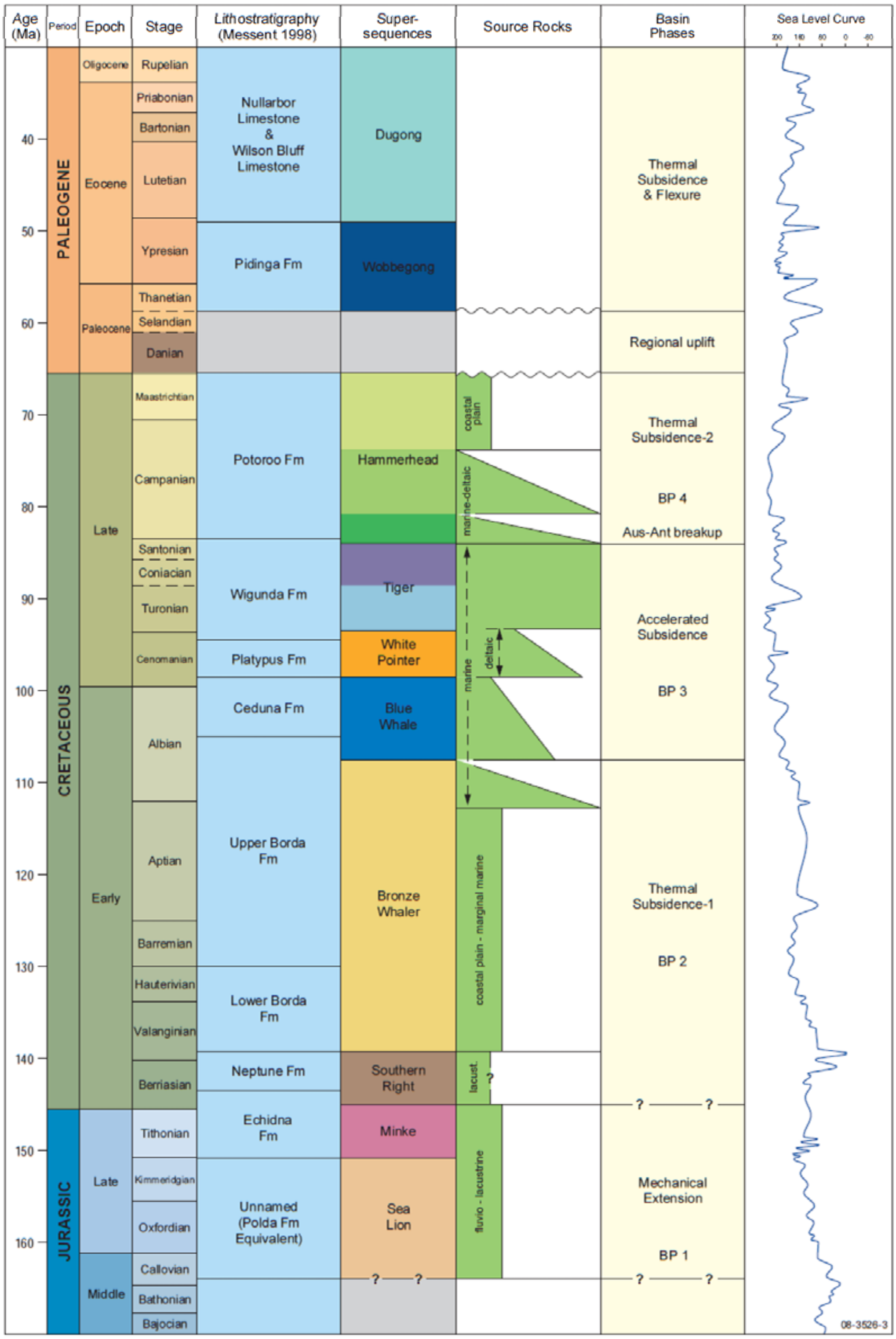

Figure 5: Bight Basin stratigraphic correlation chart showing basin phases and predicted source rock intervals (modified from Blevin et al., 2000 and Totterdell et al., 2000). The sea level curve (Haq et al., 1988) is modified to the time scale of Gradstein et al., 2004.

Exploration history

Petroleum exploration in the eastern Bight Basin (Eyre, Ceduna and Duntroon sub-basins) has occurred in three major cycles – the late 1960s to early 1970s, the early 1990s, and 2000–present (see O'Neil, 2003). After nearly fifty years of exploration in the offshore Bight Basin, only fourteen petroleum exploration wells have been drilled; Apollo-1 (1975), Borda-1 (1993), Columbia-1 (1982), Duntroon-1 (1986), Echidna-1 (1972), Gemini-1/1A (1975), Gnarlyknots-1/1A (2003), Greenly-1 (1993), Jerboa-1 (1980), Mercury-1 (1981), Platypus-1 (1972), Potoroo-1 (1975) and Vivinne-1 (1993). With the exception of Gnarlyknots-1/1A, all wells have been drilled in relatively shallow water near the basin margin. No significant hydrocarbons have been discovered and the deep-water parts of the basin remain largely untested and a frontier area.

During the last phase of exploration in the 2000s, exploration permits were awarded to a joint venture operated by Woodside Energy in the Ceduna Sub-basin. The joint venture acquired approximately 15,400 line km of 2D seismic data and in 2003, drilled Gnarlyknots-1/1A (Tapley et al., 2005). The well was the first and only attempt to test the deep-water Ceduna Sub-basin and failed to reach its primary target objective due to adverse weather conditions.

In 2007, Geoscience Australia embarked on a regional geological and sampling survey of the Bight Basin as part of the Australian Government's Offshore Energy Security program. The survey targeted and sampled potential source rocks of late Cenomanian to early Turonian age on the northwest margin of the Ceduna Sub-basin. Analytical results indicated that the organic-rich rocks recovered by the survey are capable of generating liquid hydrocarbons (Totterdell et al, 2008; Totterdell & Mitchell, 2009). In 2009, six areas in the central Ceduna Sub-basin were made available for bidding and, in January 2011, BP Developments Australia Pty Ltd was awarded four permits (EPP 37–40).

Petroleum geology

The eastern part of the Bight Basin (Ceduna, Eyre and Duntroon sub-basins) is potentially one of the most prospective deepwater frontier basins in offshore Australia. The thick sedimentary succession, in excess of 15 km thick in places, and its evolution from local half grabens depocentres during the Jurassic, to an extensive sag basin in the Early Cretaceous and passive margin during the Late Cretaceous to Holocene, implies that there is significant potential for the presence of multiple petroleum systems.

The most prospective petroleum systems are believed to be associated with thick mid to Late Cretaceous deltaic and marine sediments (Blue Whale, White Pointer, Tiger and Hammerhead supersequences), which provide reservoirs, seals and potential oil-prone source rocks at several stratigraphic levels (Figure 5), together with a wide range of structural and stratigraphic plays (Blevin et al., 2000; Totterdell et al., 2000; Struckmeyer et al., 2001; Totterdell et al., 2008) – Figure 5.

Despite mounting evidence for oil-prone marine source rocks in the Ceduna Sub-basin (Totterdell et al., 2008), and speculation they might be present in distal facies of deep water areas in the Ceduna Sub-basin, hydrocarbon generation is a key uncertainty for explorers.

Source rocks

The key interpreted source rock intervals in the Bight Basin were deposited during a transgressive half-cycle which lasted from 165 to 84 Ma and was principally controlled by the propagation of the Southern Rift System from west to east (Stagg et al., 1990). Transgressive sequences began with non-marine facies of Callovian to Berriasian lacustrine shale, grading upwards into Valanginian to mid-Albian coastal plain and marginal marine facies composed of coal, sandstone and siltstone, and finally into fully marine facies of mid-Albian to late Santonian sandstone, siltstone and shale (Blevin et al., 2000). Therefore, the oldest potential source rocks in the Bight Basin are interpreted to be lacustrine and other non-marine facies within the Upper Jurassic to lowermost Cretaceous syn-rift succession of the Sea Lion and Minke Supersequences (Geoscience Australia, 2010). Indeed, algal-rich lacustrine shales from these supersequences are interpreted as the source for a breached palaeo-oil accumulation identified from oil stains in the *Jerboa-1* well in the Eyre Sub-basin (Totterdell et al., 2000; Ruble et al., 2001).

In the overlying Southern Right Supersequence, fluvio-lacustrine claystone, siltstone and sandstone has been noted and interpreted to reach a maximum thickness of 1500 m in the Ceduna Sub-basin (Geoscience Australia, 2010). However, based on sparse Total Organic Carbon (TOC) and Rock-Eval data, this supersequence appears to have low potential for generating liquid hydrocarbons (Geoscience Australia, 2010). The final lacustrine sedimentary units belong to the overlying Bronze Whaler Supersequence, which is composed of a dominantly terrestrial lower section and a more marine-influenced upper section (Geoscience Australia, 2010) due to the incursion of marine waters into the evolving seaway between Australia and Antarctica. The lower, non-marine section is deemed to only have moderate propensity for mainly gas and limited oil generation. The more marine-influenced upper sections, by contrast, are regarded as having a much better potential for both oil and gas generation due to higher algal contributions of organic matter. Due to the variation in the relative inputs of marine and non-marine organic matter, it has been speculated that the Bronze Whaler Supersequence would have generated mostly waxy oils and gas, although an increase in marine influence towards the basin depocentre may have resulted in the generation of lighter oil (Geoscience Australia, 2010).

The onset of marine conditions in post-rift sections of the Bight Basin appears to coincide with a first- or second-order rise in global sea level between 134 and 90 Ma, suggesting a possible connection with open-marine conditions along the western Australian margin (Blevin et al., 2000). The rise in global sea level also partially coincides with a period of accelerated subsidence from 97 to 84 Ma, attributed to possible lower crustal processes (Blevin et al., 2000; Totterdell et al., 2000). It is in this setting that the Blue Whale Supersequence, comprising marine siltstone and mudstone, was deposited. This supersequence could exceed 2500 m in thickness in the centre of the Ceduna Sub-basin, with Rock-Eval and TOC data showing good potential for both oil and gas generation (Geoscience Australia, 2010) in samples recovered from the proximal wells in the basin. In the well Platypus-1, both coaly and shaly facies of this supersequence are deemed to have good oil-source potential (Geoscience Australia, 2010).

The White Pointer Supersequence consists of strata deposited in a deltaic environment, comprising fluvial to lagoonal siltstone and claystone. TOC, Hydrogen Index (HI), and Rock-Eval data from several wells indicate that the source potential of this supersequence ranges from good to excellent for both oil and gas. Coaly intervals found in this supersequence are likely to have produced waxy oils (Geoscience Australia, 2010).

The Tiger Supersequence was the final sequence deposited in the transgressive half-cycle and consists of strata deposited in marginal marine to marine settings and reaching a thickness of up to 4000 m in the Ceduna Sub-basin. Currently, only sparse geochemical data exists for this supersequence. Existing TOC and Rock-Eval data from wells drilled through proximal facies indicate poor to fair source potential. However, further basinward, seismic data interpretations infer the presence of thicker shale sequences that may have greater source potential (Geoscience Australia, 2010). Indeed, dredge samples obtained in 2007 from more distal facies of the Eyre Terrace demonstrated the presence of an excellent marine, oil-prone source rock at the base of the Tiger Supersequence (Totterdell et al., 2008; Boreham, 2009).

An important factor to consider during this transgressive half-cycle is that the mid to Late Cretaceous coincides with several global episodes of enhanced organic carbon burial, so called Oceanic Anoxic Events (OAEs; Schlanger & Jenkyns, 1976; Jenkyns, 1986; Arthur et al., 1987; Schlanger et al., 1987). During these short-lived events, elevated primary productivity is generally credited with causing an increased flux of planktonic material to the seafloor, thereby favouring the preservation of this organic matter in areas of oxygen-poor bottom water conditions (Kuypers et al., 2002). OAEs are, among other features, characterised in stratigraphic sections by black shale deposits featuring elevated organic-carbon levels (e.g. Jenkyns & Clayton, 1986). The most significant of all OAEs occurred during the late Cenomanian to early Turonian and is designated as OAE2 (Schlanger et al., 1987). While the majority of records for OAE2 were derived from sediments in the Northern Hemisphere, the occurrence of organic-rich Cenomanian/Turonian sediments at ODP Site 1138 on the Kerguelen Plateau in the southern Indian Ocean (Mohr et al. 2002; Meyers et al. 2007) suggests that mid-Cretaceous anoxic conditions extended to high southern latitudes and that OAE2 affected the entire global ocean (Boreham, 2009). Organic-rich samples recovered from the Eyre Terrace and the Tiger sequence are interpreted to have been related to the OAE2 event due to the presence of dinocyst assemblages composed of morphological variants of *Cribroperidinium edwardsii*, *Cyclonephelium compactum, Eurydinium ingramii* and *saxoniense,* which are associated with the OAE2 in both Hemispheres (Marshall & Batten 1988). In addition, these samples contain strong geochemical signatures of marine anoxia and the presence of age-diagnostic biomarkers (e.g. C26 demethylsterane) consistent with Cenomanian/Turonian (C/T) age (Totterdell et al., 2008).

After the transgressive half-cycle that produced OAE2, a change to regressive environments occurred in the late Santonian between 84 and 65 Ma (Blevin et al., 2000). The start of this half-cycle coincided with the proposed breakup between Australia and Antarctica (Veevers et al., 1991; Sayers et al., 2001, 2003). It was during this time that a large progradational delta, known as the Hammerhead Supersequence, formed. This delta, representing 19 million years of sustained sedimentary deposition, is characterised as sand-rich with strongly progradational stratal geometries (Totterdell & Krassay, 2003).

The Hammerhead Delta is subdivided into three sequence sets, with the lower two (Late Santonian to Campanian) exhibiting strongly progradational geometries, and the upper sequence set (Maastrichtian) aggradational geometries due to, firstly, an increase and, later, a decrease in sediment supply (Totterdell & Krassay, 2003). Core and cuttings and well logs of the supersequence revealed amalgamated sandstone, interbedded claystone-sandstone and massive mudstone units of the Potoroo Formation or its lateral equivalent, the Nurina Formation. In proximal parts of the basin, the Hammerhead Delta consists mainly of amalgamated fluvial channel sandstones, while distal parts consist of basinward-thinning wedges of marine shale at the toe of slope. Between these two end members, 14 other mappable seismic facies have been interpreted to represent coastal and deltaic plain, shallow marine and shelf-margin to slope palaeo-environments. A reduction in

sediment supply at the end of the Cretaceous resulted in the abandonment of deltaic deposition and the onset of a cool-water carbonate margin (Totterdell & Krassay, 2003). Little is known about source rock potential of the deltaic Hammerhead sequence and it remains grossly under sampled. However, it is likely to contain more gas-prone source rocks and coals that are typically associated with deltaic and shallow marine sequences.

Hydrocarbon indications and shows

None of the wells drilled in the Bight Basin have encountered either potential or proven hydrocarbon zones (oil or gas), and hydrocarbon indications and shows are infrequent (Table 1). The only significant oil shows reported are from Greenly-1 (Greenly-1 well completion report), which recovered oil, as a surface scum from a water/oil mixture, and gas (repeat formation test at 4209.2 m). At the time, these represented the first major indications of hydrocarbons in the basin, indicating the presence of an effective source rock, and thereby significantly upgraded the prospectivity of the Ceduna Sub-basin.

Apart from Greenly-1, none of the other wells in the Ceduna and Duntroon sub-basins revealed convincing evidence for hydrocarbon shows. This is particularly relevant for the current phase of exploration in the Bight Basin that centers on exploration permits in the deeper parts of the basin. Only one well, Gnarlyknots-1A, tests this area. While oil, potentially from synthetic-based mud fluorescence, and gas indications were minor, this provided a unique opportunity to test the hydrocarbon generation and migration potential of the area by using fluid inclusions as a tool to access potential hidden oil shows through the GABRP Project 5.3; the results of which are summarised within Box 1.

Table 1: Hydrocarbon indications and shows.

Well	Year	TD (mRT)	HC shows	Comment	Formation	Interval (mRT)
Borda-1	1993	2800	None reported	–	–	–
Duntroon-1	1986	3515.6	L1 - oil indication	Fluorescence	Upper Borda	3061; 3200
Echidna-1	1972	3832	L1 - oil indication	Black soft bituminous material, fluorescence	Lower Borda	2648; 2652
Gnarlyknots-1/1A	2003	4736	L1 - oil indication* G1 – gas indication L1 - oil indication*	Fluorescence Trace C_4 Fluorescence	Wigunda Wigunda Wigunda	4379-4712.5 (SWC) 4505-TD; max 4710 4685-4725
Greenly-1	1993	4860	L1, L2 – strong oil indications	Fluorescence	Wigunda	3430-4542 (SWC, Cuttings)
			L1 - oil indication	Fluorescence	Platypus	4770-4818
			L3, G3 – oil/gas show	Recovered oil as surface scum and water/oil mixture; gas recovered	Wigunda	4209.2 (RFT)
Jerboa-1	1980	2538	None reported	–	–	–
Platypus-1	1972	3893	None reported	–	–	–
Potoroo-1	1975	2924	G1 – gas indication	18,000ppm C_1	Platypus	2128-2132
Vivonne-1	1993	3000	None reported	–	–	–

Data summarised from Messent (1998). RFT = repeat formation test. SWC = side-wall core. * Considered likely to be synthetic-based mud fluorescence. L1 = oil indication (fluorescence or cut); L2 = strong oil indication (fluorescence or cut & other oil indication e.g. log anomaly); L3 = oil show (oil recovered from core, test, mud); L4 – potential oil zone (oil show with convincing log anomaly); L5 = proven oil zone (oil flow on test or RFT & log anomaly proving accumulation). G1 = gas indication (anomalously high gas readings); G2 = strong gas indication (anomalously high gas readings and other indications e.g. core, logs or shakers); L3 = gas low on tests; L4 = potential gas zone (gas show with convincing log anomaly or other indication); L5 = proven gas zone (sustained gas flow on test or RFT and log anomaly or pressure data proving an accumulation).

Box 1

Summary findings of GABRP Project 5.3 fluid Inclusions project

Thirty six samples from 7 exploration wells (Borda-1, Duntroon-1, Greenly-1, Jerboa-1, Platypus-1, Potoroo-1) including the previously untested Gnarlyknots-1A well were analysed using CSIRO's Grains with Oil Inclusions (GOI™) technique. These analyses identified not only oil-bearing, but in some samples gas-rich, inclusions at low abundance (GOI <0.7%, up to a maximum of 1.1% in Greenly-1) (Kempton et al., 2017). This is positive evidence for widespread oil and gas generation and migration in the Bight Basin. Oil indications are more frequent in intervals from the Late Cretaceous White Pointer, Tiger and Hammerhead supersequences.

Geochemical hydrocarbon fingerprints generated using CSIRO's Molecular Composition of oil Inclusions (MCI) and gas-isotope techniques were performed on minute quantities of oil and gas extracted from the fluid inclusions. Fluid inclusion (FI) oil from Gnarlyknots-1A (4390–4425 m; Tiger Supersequence) comprises a mixture of types including oil and gas-condensate. The *n*-alkane and biomarker characteristics show a mixed organic matter input from both algae and terrestrial plants and was generated from source rock(s) deposited in suboxic-oxic marine environment(s). The wide range of maturities, 0.65–1.3% VRE, in the FI oil suggests either a mixture of oils generated from different source rocks (Blue Whale and Tiger having potential marine algal inputs, while the White Pointer has potential terrestrial plant input), or from the same source rock at different maturity stages – perhaps an unrecognised paralic facies of the White Pointer, containing both algal and terrestrial organic matter. The gasoline-range hydrocarbons are dominated by toluene and originated, in part, from coeval aqueous inclusions. The bulk $\delta^{13}C$ isotopic composition of methane (-28.4 and -28.6 ‰ replicates) and ethane (-17.6 and 18.1 ‰ replicates) indicates a thermogenic origin for these hydrocarbon gases, probably derived from Type III (humic/coaly) organic matter.

By comparison, FI oil from Greenly-1 (4806-4818 m; White Pointer Supersequence) is from oil inclusions only, with no gas-condensate visually detected. The *n*-alkane and biomarker characteristics indicate significant organic matter input from terrestrial plants, and a minor contribution from a lacustrine source, and was generated from a source rock deposited in an oxic, clay-rich fluvio/deltaic depositional environment. This FI oil represents a pristine oil sample that was generated over a narrow maturity range at the early to peak oil window (0.8–1.1% VRE), and lacks the mixed algal input associated with other oil show extracts from the same well. Previous correlations of these oil shows to the Bronze Whaler source sequence are potentially not supported by the lack of algal input to the FI oil, and suggests the White Pointer may be a better source sequence.

To understand the timing of oil migration, the pressure-temperature (*PT*) trapping conditions of hydrocarbon inclusions were determined in Gnarlyknots-1A, Greenly-1, Duntroon-1 and Potoroo-1. The intra-Coniacian primary well target in Gnarlyknots-1A (4410-15 m; Tiger Supersequence) was a migration pathway, over an extended period of time, for a variety of hydrocarbon fluid compositions modelled by Petroleum Inclusion Thermodynamic (PIT) as black

oil, light oil, gas-condensate and gas + CO_2. There is good concordance in the measured *PT* data with independent *PT* curves from basin models. The earliest oil entrapment took place at a minimum of 58°C, with constrained *PT* conditions of light oil (240–270 bar; 69.2°C) in the Late Cretaceous at ~70–75 Ma (Campanian). Phase separation of light oil, and entrapment of both gas-rich phases and gas-depleted black oil, occurred at *PT* conditions (285–308 bar; 80-85°C) in the Late Cretaceous at ~70 Ma (Maastrichtian). Subsequent entrapment of gas-condensate took place at pressure conditions (350–410 bar @ 80°C) reached at ~35–15 Ma (Oligocene to Early Miocene), followed by gas + CO_2 at *PT* conditions (370–408 bar; 78–88°C) reached at ~27–15 Ma (late Oligocene to Early Miocene). This apparent sequence of hydrocarbon entrapment from oil to gas over time might simply be explained by generation from a single source rock over a range of thermal maturity stages (i.e. paralic facies of the White Pointer?). Late black oil entrapment, at pressure conditions (400 bar) reached at ~18 Ma (Miocene), might be from a different source rock that entered the oil window later in the basin history.

The Cenomanian interval in Greenly-1 (4808–12 m; Tiger Supersequence) trapped remarkably consistent hydrocarbon assemblages modelled by PIT as black oil. While this consistency is also reflected in the measured *PT* entrapment conditions (270–340 bar; 127–135°C), they are not concordant with the independently modelled *PT* curve. If the temperatures reflect the entrapment conditions, then this constrains oil charge to the early Miocene (~23–5 Ma) and at a depth equivalent to about 2 km less that modelled. Tertiary carbonate progrades over the Late Cretaceous deltas, and rapid burial peaking around 15 Ma, may go some way to explaining this. More recent charge from the White Pointer source sequence, due to recent sediment loading, is consistent with this timing and is potentially supported by the MCI result. If, however, the pressures reflect the entrapment conditions, then this constrains oil charge in Greenly-1 to the Campanian–early Eocene (~75–52 Ma) and at temperatures about 30°C higher than modelled. One explanation might be a transient period of hotter fluids that were in thermal disequilibrium with the rock.

The Turonian-Santonian interval in Duntroon-1 (2505–10 m; Tiger Supersequence) and the Cenomanian-Santonian interval in Potoroo-1 (1778–86 m; Tiger Supersequence) were migration pathways for a variety of hydrocarbon fluid compositions modelled by PIT as black oil, light oil and, in the case of Duntroon-1, gas (+ N_2 and CO_2). In both these wells located on the margins of the basin, hydrocarbon charge appears to be late. Because pressure evolution over much of the Cenozoic in Duntroon-1 was static, temperature constraints (81–95°C) suggest entrapment from the mid-Miocene (~17 Ma) to recent. The presence of CO_2 and N_2-rich hydrocarbon gases may have volcanic origins similar to those from the Otway Basin. In Potoroo-1, hydrocarbon entrapment occurred either from the Oligocene (~32 Ma), or from the early Miocene (~25 Ma), to recent. Because of its location up-dip of the central Ceduna depocentre, a variety of potential source/charge scenarios could be envisaged including earlier re-migrated oil.

Historical bitumen strandings

In addition to hydrocarbon shows and fluid inclusion studies there has been long standing evidence for bitumen strandings on the beaches of the southern margin of Australia, which could be indicative of active offshore petroleum system in the GAB. Concise summaries of the historical literature on Australian coastal bitumen may be found in Sprigg & Woolley (1963), Padley (1995) and Edwards et al., (2016). The following resumé draws heavily on these sources.

Records of bitumen being washed ashore along the coasts of western and southern Australia date back to the mid-1800s when pioneering sealers and whalers collected this material to caulk their boats (Howchin, 1903; Ward, 1944; Sprigg, 1983). While some of the earliest reports may be found in colonial newspapers, the first official record of coastal bitumen in Australia is contained in a report to the South Australian Surveyor-General. In his capacity as the colony's Mineral Surveyor, Trewartha (1850) reported finding on the beach at Vivonne Bay, Kangaroo Island, several hundredweight of bitumen in large and small pieces, none of which appeared to be water-worn. The bitumen in question was 'asphaltum', later to become known as asphaltite. Tolmer (1882) likewise refers to the 'asphaltum' he found on the southern coast of Kangaroo Island in August 1844. Further east, in Victoria, coastal bitumen had been found near Portland and at the mouth of the Bass River in Westernport Bay, some of the latter specimens being noted to "resemble tar" (Brough-Smyth, 1869). 'Asphaltum' is the most common variety of Tasmanian coastal bitumen (Hills, 1914; Twelvetrees, 1915; Wade, 1915). The 'asphaltum' described by Twelvetrees (1915) appears to physically resemble that which washes ashore in South Australia.

A review of the historical literature (Edwards et al., 2016) revealed that a diverse terminology has been employed to describe what appear to be five distinct varieties of Australian 'coastal bitumen':

Waxy bitumen, bitumen, tarballs;

Weathered waxy bitumen, oxidised crude, flaky crude;

Asphaltite, asphaltic bitumen, asphaltum, asphalt, manjak, pitch, mineral pitch, dammar;

Oil slick, oil, oily material, crude, sticky tar, kerosene; and

Wax, ozokerite, paraffin wax, mineral wax, earth wax.

From their descriptions, it is apparent that these stranded bitumens were not of uniform physical appearance, varying from solid to semisolid and liquid states. It is worth noting that the lack of a standard descriptive terminology has, in many instances, made it difficult to decipher exactly what substances were found. Bold type highlights the preferred terminology that will be adopted in this report and subsequent publications.

Early reports of stranded tarballs and 'asphaltum' (the two most common varieties) are not restricted to the southern Australian mainland. Other localities include Elcho Island, Northern Territory (Wade, 1924; Hunter, 1964); Mandurah and between Cape Arid and Doubtful Island Bay, Western Australia (Tate, 1883; Sprigg & Woolley, 1963); and the west and south coasts of Tasmania (Hills, 1914; Twelvetrees, 1915, 1917; Wade, 1915; Ward, 1944). Even further afield, similar petroleum substances have been found on the beaches of New Zealand, Chile, South Africa (Ward, 1944) and, more recently, the Seychelles (Plummer, 1996).

Historically, the stranding of coastal bitumen has been reported most frequently at localities in South Australia on the southern Eyre and Yorke Peninsulas, on Kangaroo Island and along the Limestone Coast; and in western Victoria, from Discovery Bay to Cape Otway (Brown, 1898; Ward, 1913; Wade, 1915; Howchin, 1919; Sprigg, 1961, 1962; Sprigg & Woolley, 1963), as highlighted in Figure 6 and Figure 7. Extending from Robe to Portland, the Bonney Coast is arguably the principal locus for bitumen stranding in southern Australia (Figure 7). By comparison, there are notably fewer reports of bitumen stranding along the coastline of the GAB (Figure 6).

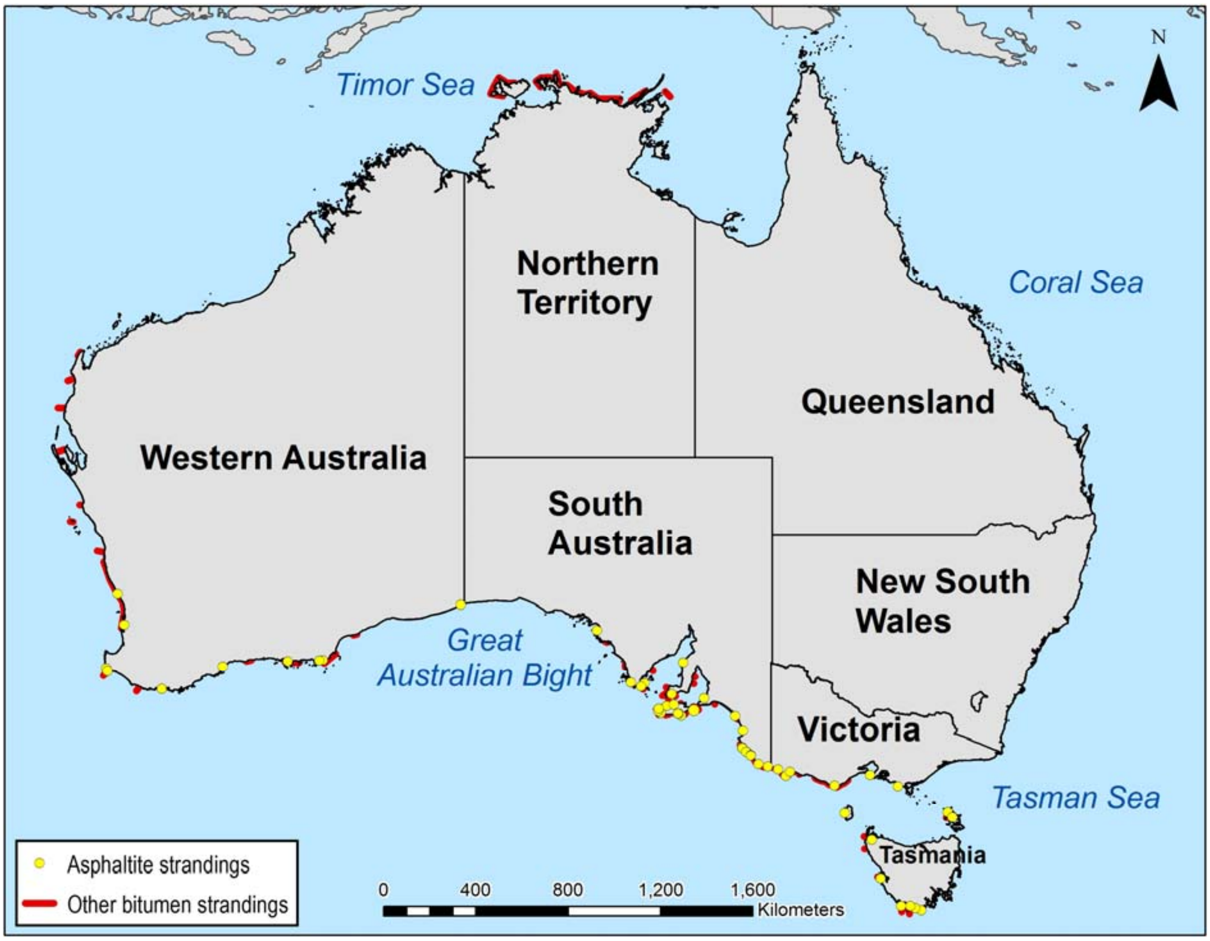

Figure 6: Location of bitumen stranding sites along the Australian coastline (after Edwards et al. 2016).

These stranded bitumens typically occur on sandy beaches close to the high-water mark, although there are exceptions. Pieces of bitumen and 'asphaltum' were found amongst sand hills up to a mile from the coast, particularly near Robe, South Australia (Howchin, 1903; Twelvetrees, 1915; Wade, 1915). A large block of 'asphaltum' was encountered 20 feet below the surface, while a well was being sunk adjacent to the Portland-Blowhole road in western Victoria (Reid, 1931).

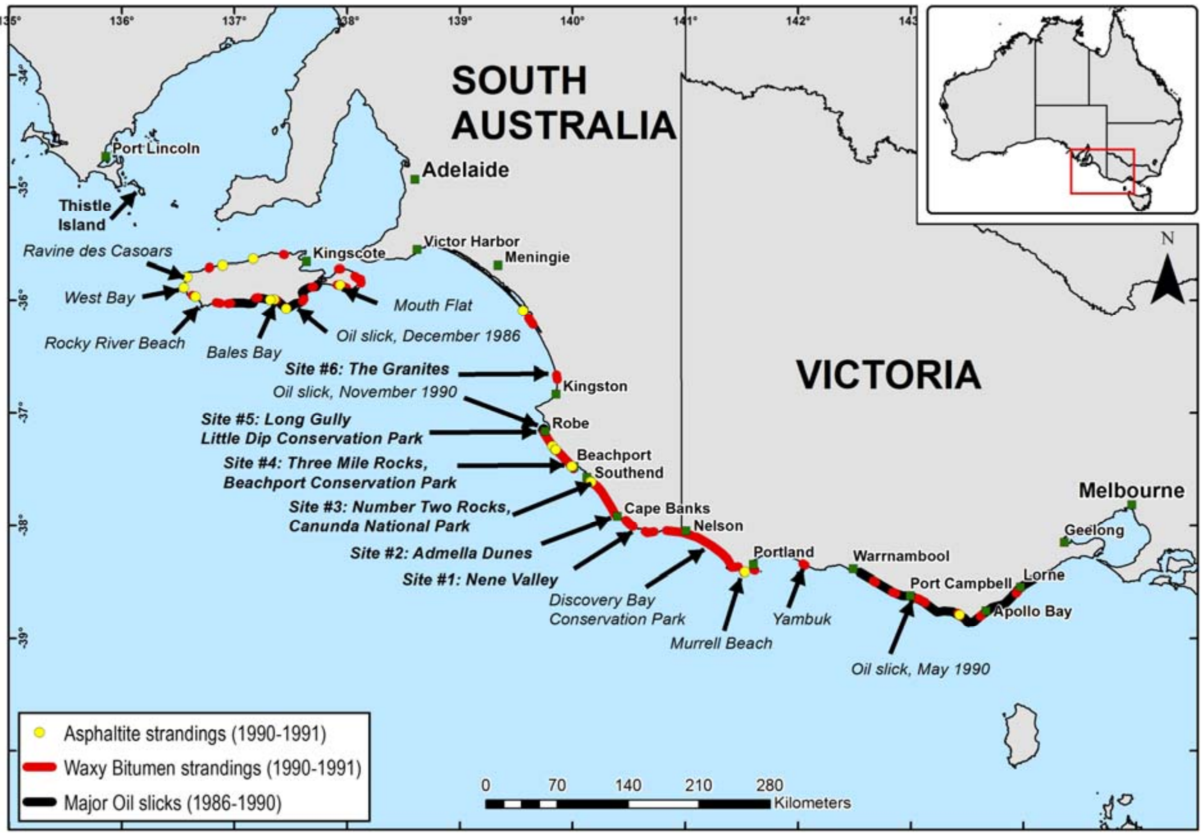

Figure 7: Stranding locations of coastal bitumen in South Australia and western Victoria (after Edwards et al. 2016).

Understandably, these early reports raised questions regarding the origin of the stranded bitumen, its likely derivation from local or distant oil seeps, and hence its possible implications for the petroleum prospectivity of the sedimentary basin in which the stranding site was located. By the time offshore petroleum exploration commenced in southern Australian waters during the early 1960s, these questions had still not been satisfactorily answered. The uncertain provenance of the bitumen strandings subsequently led to a series of detailed geochemical investigations aimed at establishing how many oil types were represented and their likely source affinities. These investigations focused on material collected from beaches in South Australia and western Victoria (McKirdy & Horvath, 1976; McKirdy et al. 1986, 1994; Padley et al. 1993; Edwards et al. 1998; Hall et al. 2014), Tasmania (Volkman et al. 1992), Western Australia (Currie et al. 1992; Alexander et al. 1994) and the Northern Territory (Summons et al. 1993). With the notable exception of those by Padley/Edwards, these more recent studies typically provided little or no information on the abundance of bitumen found at a given site, its position on the beach, and the shape, size, weight and physical appearance of the individual specimens collected.

In 1983 the South Australian Department of Mines and Energy (SADME) conducted a major survey of stranded bitumen along the South Australian and western Victorian coastline, involving the collection of new samples for geochemical analysis (McKirdy, 1984a, b), with a view to promoting petroleum exploration within the adjacent offshore Otway and Duntroon Basins. The same agency sponsored follow-up beach surveys during 1990–1992 as part of a PhD project (Padley, 1990, 1992, 1995). The

latter study was the first to yield a quantitative estimate of the natural hydrocarbon loading of Australian ocean beaches (as documented in Edwards et al., 2016).

Evidence for seeps

To attempt to identify the source of some of the asphaltites and help de-risk offshore hydrocarbon exploration, several seepage studies have been conducted within the GAB, primarily focusing on the Ceduna sub-basin. These have included remote sensing synthetic aperture radar (SAR) data collection, seismic interpretations and vessel-based investigations.

Remote sensing and seismic studies

Remote sensing studies were undertaken in the GAB by Australian Geological Survey Organisation (AGSO, now GA) both in 1999 (Stuckmeyer, 2000) and 2005/2006.

These combined studies collected 201 synthetic aperture radar (SAR) captures over the wider GAB, using a combination of European remote sensing satellite (ERS) and RadatSat SAR satellite platforms, to evaluate hydrocarbon migration and seepage. Within these captures 183 SAR anomalies were identified, none of which were interpreted as high confidence slicks (ranked 2 and below). Seventeen slicks were identified as rank 2 slicks with moderate confidence, and 97 as rank 3 slicks (lowest rank) with moderate to low confidence. All other SAR anomalies were assigned to remnant pollution or natural films (Figure 8).

These data were compared with legacy airborne laser fluorosensor (ALF) and 2D seismic data to provide an assessment of the likely charge characteristics of the region. The results of the study suggested that there was active liquid seepage with the Great Australian Bight basin system albeit restricted. Direct correlation of the individual seeps with geological features was not possible as none of the reported seep locations coincided with subsurface fluid escape features identified from the limited seismic data available in the basin at the time.

The high proportion and distribution of the SAR anomalies identified in the west of the Ceduna sub-basin in EPP 43 during the 2005/2006 capture campaign was distinctly different from those encountered in the 1999 acquisition program data. In part these data were used in the planning of the seeps directed activities of the R/V Southern Surveyor Survey SS01/2007.

These remote sensing studies have highlighted that slicks were more abundant across the NW Shelf than in the GAB. This may be due to a number of reasons:

- Differences in water depth, swell height and water temperature – an example being consistently high swells that may account for the small size and scattered nature of slicks;
- High seal and trap integrity in the greater part of the GAB basin system;
- Low number of seeps could reflect a low density of hydrocarbon accumulations; and
- Episodic hydrocarbon leakage (Struckmeyer, 2000)

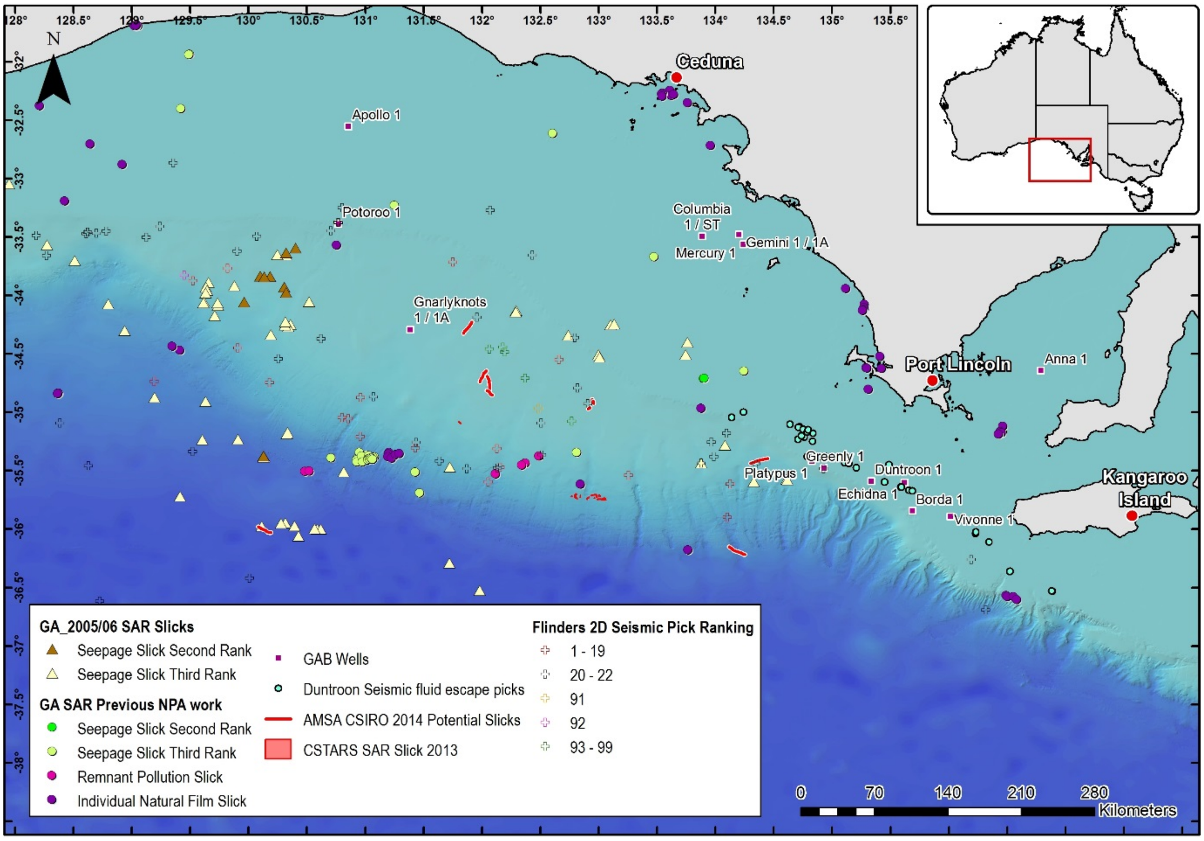

Figure 8: Combined historical and capture program (SAR Slick Features) sea surface synthetic aperture radar anomalies for the Great Australian Bight, plus seismic indications of fluid escape in the Duntroon sub-basin.

Vessel-based investigations

There have been eight known prior marine research surveys undertaken by Geoscience Australia and CSIRO studying aspects of the geology of the GAB between 1989 and 2013. Whilst these surveys have collected numerous samples across the bight (Figure 9) where samples have been geochemically characterized none have identified thermogenic hydrocarbons indicative of deep source seepage.

Only two of the eight research surveys in the GAB have specifically attempted to delineate hydrocarbon seepage (viz. SS01/2007; Totterdell & Mitchell 2009; ss2013_C02, Williams et al., 2013a,b). Whilst the number of marine surveys performed in the GAB appears to be numerous, only recent advances in marine survey technologies, and the collection of new seismic and remote sensing data sets have permitted a more detailed understanding of the GAB geology and planning of a more precise survey.

The ss2013_C02 voyage was primarily focused on benthic and pelagic ecology studies with only limited acoustic reconnaissance opportunities undertaken for the delimitation of potential seepage (using sub-bottom profiler, single beam echo sounder water column acoustics and multibeam echo sounder swath mapping (Williams et al., 2013b)). These operations predominantly occurred at the transition between deepwater to abyssal slope between 131°5'-133°E and 35°-36°S. The sites investigated were selected on the basis of 2D seismic data and synthetic aperture radar captures

concurrent with the voyage, which identified potential sea surface slicks (see Box 2, Figure 8). Several low rank acoustic anomalies were identified during this voyage within both the sub-bottom profiler data and the single beam echo sounder data, although these data are equivocal (Ross et al., 2017).

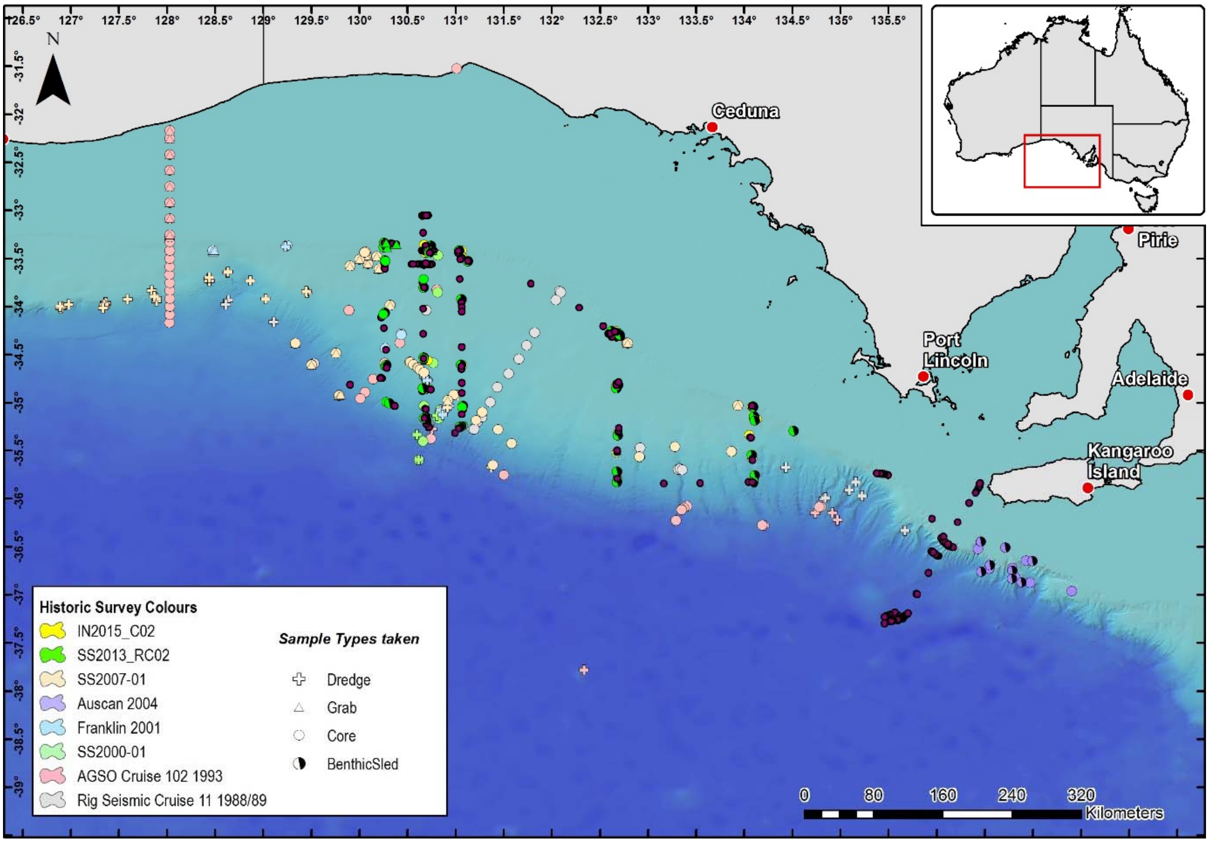

Figure 9: Combined historic seafloor sampling sites from surveys undertaken in the Great Australian Bight.

The ss201/2007 multifaceted Geoscience Australia led survey (Totterdell & Mitchell, 2009) aimed to investigate potential natural hydrocarbon seepage at sites across the Ceduna sub-basin, which could provide evidence for the presence of active petroleum systems. The survey investigated six potential seepage locations (Areas 1-3, 7-9, Figure 10) selected on the basis of geophysical and remote sensing seepage indicators (Totterdell & Mitchell, 2009).

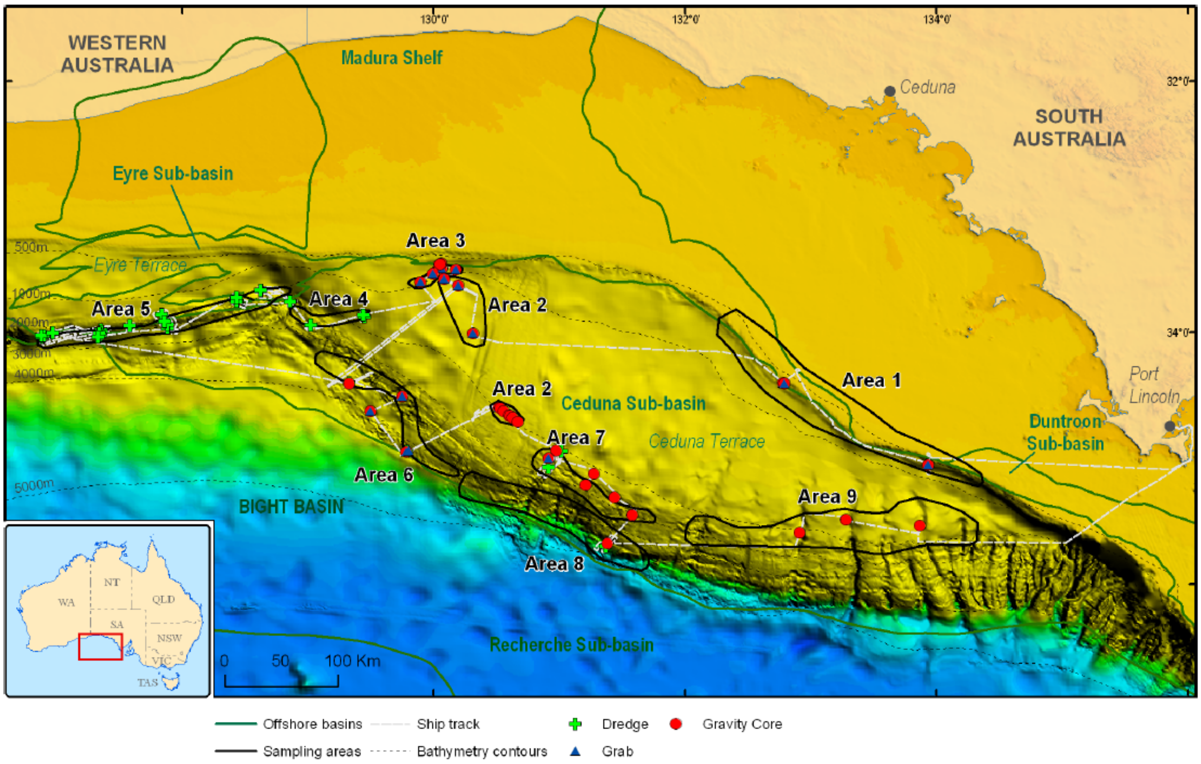

Figure 10: Bight Basin Sampling and Seepage Survey SS01/2007: survey areas and location of sampling sites (Totterdell & Mitchell, 2009).

These sites were initially characterised using acoustic methods, namely a hull-mounted single dual-frequency echo sounder for the detection of water column hydro-acoustic flares and a multibeam echo sounder system for bathymetric mapping. Shallow subsurface geophysical data were also collected through the use of a sub-bottom profiler system. Detailed site characterisation was achieved using a towed video camera system and side-scan sonar system (Area 1) only. Sediment samples were collected with a combination of grab, dredge and coring techniques for detailed geochemical investigation, including headspace gas and high-molecular-weight hydrocarbon analysis.

Data collected within Area 1 and on the transit to Area 2 delineated a number of potential seep-related features, including areas of high seabed reflectivity observed in side-scan sonar data, potential hydro-acoustic flares and amplitude anomalies within sub-bottom profiler data. These features were observed in the vicinity of subsurface faulting and SAR slick anomalies. However, sampling within these areas failed to identify thermogenic hydrocarbons in both the headspace gas and the high-molecular-weight hydrocarbons.

Multibeam swath data collected within Area 3 allowed mapping of reactivated underlying basin margin faults which form seafloor scarps. An area of seabed with circular depressions was identified on a plateau in the northern part of Area 3 at a water depth of about 700 m. These depressions, ~150 m in diameter and 5 m deep, are located on a ~5° SE slope. These features were interpreted by Totterdell & Mitchell (2009) to be possible pockmark features related to fluid escape that is currently active, or alternatively recent palaeo-fluid escape features. Once again sampling of these features and geochemical analysis of the samples failed to positively detect thermogenic hydrocarbons.

The remaining areas studied during the SS01/2007 voyage failed to unequivocally identify seepage and Totterdell & Mitchell (2009) cite several possible reasons for this, including hydrocarbons not being preserved in the very shallow section (<10 m) that was sampled by the gravity corer, poor targeting of potential seepage sites, or the lack of any hydrocarbon seepage. In particular they advocate for the use of equipment capable of taking deep cores in order to access deeper intervals where hydrocarbons may be present.

Box 2

Seepage indicators from GABRP Project 5.1 seeps and leakage project.

To identify potential sites of hydrocarbon seepage a multidisciplinary approach was taken. Of the 81 areas of interest identified from the rapid screening of 2D seismic data for leakage indicators within the Ceduna sub-basin (Figure 8) no one area displayed unequivocal evidence of fluid leakage through the subsurface to the seafloor (Ross et al., 2017).

Sea-surface slick studies included the acquisition of four additional SAR scenes which augmented the 231 publically available scenes. Twenty three sea-surface anomalies were identified within the four additional scene captures which clustered in proximity to anomalies identified in prior scene captures. These data were used, in conjunction with the areas of interested identified for 2D seismic data screening, to determine areas for subsequent reconnaissance on the SS2013_C02 voyage.

Of the areas studied during the SS2013_C02 voyage and the subsequent IN2015_C02 voyage, there is only weak evidence for possible seepage from the data collected, in part due to the very limited time spent on these activities as part of the voyages. This outcome is not a definitive indication of the absence of seepage in the basin, as the basin comprises a very large area.

Of the 84 samples that were collected during the SS2013_C02 voyage (Figure 8) and by a 2013 BP chartered *M/V Fugro Southern Supporter* voyage, quantitative analysis of seawater extracts indicated that polycyclic aromatic hydrocarbons (PAHs) are largely absent in and around the BP permits in the GAB. Naphthalene, a highly volatile bicyclic aromatic hydrocarbon, detected in small amounts in the majority of the samples, is probably a contaminant cumulatively inherited from solvents, glassware and/or unknown source(s).

The qualitative organic geochemical analyses of extractable organic matter isolated from seawater, seabed sediment, and GO net samples, and headspace gases extracted from multicore/piston core samples collected from the GAB region indicate that petroleum hydrocarbons are either absent or below the limits of detection, pointing to an absence of active hydrocarbon seepage in and around the sampling region. The trace amounts of themogenic hydrocarbons found in two water samples and a GO net sample are likely to be inherited from a contaminant oil of an unknown source.

The seabed sediment samples contain variable amounts of extractable organic matter (0–3200 ppm) in which there are no detectable petroleum hydrocarbons (Ross et al., 2017).

Formation of coastal bitumen and potentially analogous systems

As no seafloor seeps for the asphaltites and waxy bitumen collected along the South Australian coastline have yet been explicitly located or characterised, the exact processes responsible for their

formation cannot be easily determined. This section provides a brief summary of the potential origin mechanisms for the Southern Australian margin asphaltites and waxy bitumen (tarballs), followed by overviews of two of the best-studied potential analogues: the Gulf of Mexico and the Santa Barbara Channel.

Proposed origin processes for South Australian asphaltites and waxy bitumen

Proposed origin of waxy bitumen

The origin of the waxy bitumen has largely been ascribed to unidentified seafloor tar seeps in the Indonesian Archipelago (Edwards et al., 2016, 2017). These bitumens, which are positively buoyant, become entrained in the ocean currents of the Indonesian Throughflow and are ultimately transported to Australia's southern margin by the Leeuwin Current (Figure 11). As the documentation of waxy bitumen strandings predates significant petroleum exploration in Indonesia and crude oil importation by tanker, the waxy bitumens are unlikely to be the result of accidental spillage (Edwards et al., 2016). However, given the presence of multiple waxy bitumen families (McKirdy et al. 1984a, b; Padley, 1995; Edwards et al., 2016, 2017), previous studies also note the possibility that some varieties of waxy bitumen, specifically those lacking botryococcane, may be derived from sedimentary basins along Australia's southern margin (McKirdy et al., 1994; Padley et al., 1995).

Proposed origin of asphaltites

Presently two competing hypotheses exist to explain the origin of the asphaltites: (1) degradation of a natural oil slick on the sea surface which progressively degrades into a tar 'mousse' before completely solidifying (Edwards et al., 1998; Logan et al., 2010) and (2) seepage of asphalt directly onto the seafloor (Hall et al., 2014). Previously the asphaltites were also hypothesised to be anthropogenic in origin, as many identified stranding sites coincided with historical whaling stations (Edwards et al., 1998). This suggested the asphaltites may have been caulking bitumen stored in casks buried on the whaling station beaches which were eroded and delivered to the ocean through storm activity. The hypothesis was similarly supported by historical accounts of the asphaltites being used to seal wooden ships. However, this interpretation has since been falsified by geochemical comparison of the asphaltites with caulking tars recovered from historical shipwrecks which revealed no relationship between them (Smart, 1999). Additionally, the continued stranding of fresh specimens suggests that their source remains active.

The degradation of a surficial oil slick to form a semi-solid bitumen was proposed by both Edwards et al. (1998) and Logan et al. (2010). This process has been documented in the Santa Barbara Channel (see analogues section below) where tar stranding is substantially greater in the summer months due to calmer sea-surface conditions which allow tar ball formation. In winter, due to wave action and winds from storms, the oil slicks break apart and are dispersed before they can form tar balls and be deposited on the shoreline (Lorenson et al., 2009). The stranding of asphaltite along the Limestone Coast also occurs predominantly during the winter months due to a combination of increased storm frequency and the dominance of the Coastal Current along Australia's southern margin (Padley, 1995; Edwards et al., 2016).